REPORT DOCUMENTATION PAGE

Form Approved OMB NO. 0704-0188

The public reporting burden for this collection of information is estimated to average 1 hour per response, including the time for reviewing instructions, searching existing data sources, gathering and maintaining the data needed, and completing and reviewing the collection of information. Send comments regarding this burden estimate or any other aspect of this collection of information, including suggesstions for reducing this burden, to Washington Headquarters Services, Directorate for Information Operations and Reports, 1215 Jefferson Davis Highway, Suite 1204, Arlington VA, 22202-4302. Respondents should be aware that notwithstanding any other provision of law, no person shall be subject to any oenalty for failing to comply with a collection of information if it does not display a currently valid OMB control number.
PLEASE DO NOT RETURN YOUR FORM TO THE ABOVE ADDRESS.

1. REPORT DATE (DD-MM-YYYY) 30-10-2009	2. REPORT TYPE Final Report	3. DATES COVERED (From - To) 1-Oct-2008 - 30-Sep-2009

4. TITLE AND SUBTITLE Final Technical Report-Development of III-Nitride Based THz Inter-Subband Lasers	5a. CONTRACT NUMBER W911NF-08-1-0459
	5b. GRANT NUMBER
	5c. PROGRAM ELEMENT NUMBER 8H20T2
6. AUTHORS M. Razeghi	5d. PROJECT NUMBER
	5e. TASK NUMBER
	5f. WORK UNIT NUMBER

7. PERFORMING ORGANIZATION NAMES AND ADDRESSES Northwestern University Evanston Campus Office of Sponsored Research Northwestern University Evanston, IL 60208 -1110	8. PERFORMING ORGANIZATION REPORT NUMBER

9. SPONSORING/MONITORING AGENCY NAME(S) AND ADDRESS(ES) U.S. Army Research Office P.O. Box 12211 Research Triangle Park, NC 27709-2211	10. SPONSOR/MONITOR'S ACRONYM(S) ARO
	11. SPONSOR/MONITOR'S REPORT NUMBER(S) 55335-EL-DRP.1

12. DISTRIBUTION AVAILIBILITY STATEMENT
Approved for Public Release; Distribution Unlimited

13. SUPPLEMENTARY NOTES
The views, opinions and/or findings contained in this report are those of the author(s) and should not contrued as an official Department of the Army position, policy or decision, unless so designated by other documentation.

14. ABSTRACT
III-Nitrides, due to their large conduction band offset and fast transition speeds, are promising constituents for intersubband (ISB) devices. In addition, III-Nitrides are characterized by a very large phonon energy (90 meV). This makes them ideally suited to the realization of near room temperature operating THz lasers. The objective of this program has been to demonstrate the potential for using III-Nitrides to realize a room temperature operating terahertz intersubband laser.

15. SUBJECT TERMS
Terahertz, III-Nitrides, Intersubband, Quantum Cascade Laser, GaN, AlGaN

16. SECURITY CLASSIFICATION OF:			17. LIMITATION OF ABSTRACT	15. NUMBER OF PAGES	19a. NAME OF RESPONSIBLE PERSON Manijeh Razeghi
a. REPORT UU	b. ABSTRACT UU	c. THIS PAGE UU	UU		19b. TELEPHONE NUMBER 847-491-7251

Report Title

Final Technical Report-Development of III-Nitride Based THz Inter-Subband Lasers

ABSTRACT

III-Nitrides, due to their large conduction band offset and fast transition speeds, are promising constituents for intersubband (ISB) devices. In addition, III-Nitrides are characterized by a very large phonon energy (90 meV). This makes them ideally suited to the realization of near room temperature operating THz lasers. The objective of this program has been to demonstrate the potential for using III-Nitrides to realize a room temperature operating terahertz intersubband laser.

As part of this contract, a comprehensive model of intersubband transitions was developed that takes into account the important effects of strain on bandstructure and piezo-as well as spontaneous- electric fields. Interband photoluminescence and intersubband absorption measurements were performed to help develop the modeling. We demonstrated the shortest MOCVD-grown III-Nitride intersubband absorption wavelength of 1.5 ?m as well as the longest intersubband wavelengths of 5.3 ?m, by any growth technique. In addition to investigating the optical properties we fabricated and tested both resonant tunneling diodes and quantum well infrared photodetectors in order to investigate quantum transport in III-Nitrides. Based on the refined III-Nitride intersubband models designs were also developed for room temperature terahertz emission via optical pumping. Electrical injection designs were also proposed for both polar and non-polar growth orientations.

List of papers submitted or published that acknowledge ARO support during this reporting period. List the papers, including journal references, in the following categories:

(a) Papers published in peer-reviewed journals (N/A for none)

C. Bayram, B. Fain, N. Pere-Laperne, R. McClintock, and M. Razeghi, Proceedings of SPIE 7222, p. 722212 (2009)

C. Bayram, N. Pere-Laperne, R. McClintock, B. Fain and M. Razeghi, Applied Physics Letters, Vol. 94, No. 12, p. 121902 (2009)

N. Pere-Laperne, C. Bayram, L. Nguyen-The, R. McClintock, and M. Razeghi, Applied Physics Letters, Vol. 95, No. 13, p. 131109 (2009)

C. Bayram, J.L. Pau, R. McClintock and M. Razeghi, Journal of Applied Physics, Vol. 104, p. 083512 (2008)

Number of Papers published in peer-reviewed journals: 4.00

(b) Papers published in non-peer-reviewed journals or in conference proceedings (N/A for none)

Number of Papers published in non peer-reviewed journals: 0.00

(c) Presentations

"Material and design engineering of (Al)GaN for high-performance avalanche photodiodes and intersubband applications," SPIE International Symposium on Microtechnologies for the New Millennium, Dresden, Germany, May 4-6, 2009

Number of Presentations: 1.00

Non Peer-Reviewed Conference Proceeding publications (other than abstracts):

Number of Non Peer-Reviewed Conference Proceeding publications (other than abstracts): 0

Peer-Reviewed Conference Proceeding publications (other than abstracts):

C. Bayram, B. Fain, N. Pere-Laperne, R. McClintock and M. Razeghi, Proceedings of SPIE, 7222, p. 7222212 (2009)

Number of Peer-Reviewed Conference Proceeding publications (other than abstracts): 1

(d) Manuscripts

N. Pere-Laperne, C. Bayram, L. Nguyen-The, R. McClintock, and M. Razeghi, "Intersubband absorption at 5.3 micron in GaN/Al(0.2)Ga(0.8)N superlattices grown by metalorganic chemical vapor deposition," submitted to Applied Physics Letters.

C. Bayram, N. Pere-Laperne, and M. Razeghi, "Effects of growth temperature and well width on optical and structural characteristics of AlN/GaN superlattices grown by metal-organic chemical vapor deposition," submitted to Applied Physics Letters.

Number of Manuscripts: 2.00

Number of Inventions:

Graduate Students

NAME	PERCENT_SUPPORTED
Can Bayram	1.00
FTE Equivalent:	**1.00**
Total Number:	**1**

Names of Post Doctorates

NAME	PERCENT_SUPPORTED
Dr. Nicolas Pere-Laperne	0.50
Dr. Ryan McClintock	0.50
FTE Equivalent:	**1.00**
Total Number:	**2**

Names of Faculty Supported

NAME	PERCENT_SUPPORTED	National Academy Member
Dr. Manijeh Razeghi	0.10	No
FTE Equivalent:	**0.10**	
Total Number:	**1**	

Names of Under Graduate students supported

NAME	PERCENT_SUPPORTED
FTE Equivalent:	
Total Number:	

Student Metrics

This section only applies to graduating undergraduates supported by this agreement in this reporting period

The number of undergraduates funded by this agreement who graduated during this period:	0.00
The number of undergraduates funded by this agreement who graduated during this period with a degree in science, mathematics, engineering, or technology fields:......	0.00
The number of undergraduates funded by your agreement who graduated during this period and will continue to pursue a graduate or Ph.D. degree in science, mathematics, engineering, or technology fields:......	0.00
Number of graduating undergraduates who achieved a 3.5 GPA to 4.0 (4.0 max scale):......	0.00
Number of graduating undergraduates funded by a DoD funded Center of Excellence grant for Education, Research and Engineering:......	0.00
The number of undergraduates funded by your agreement who graduated during this period and intend to work for the Department of Defense	0.00
The number of undergraduates funded by your agreement who graduated during this period and will receive scholarships or fellowships for further studies in science, mathematics, engineering or technology fields:......	0.00

Names of Personnel receiving masters degrees

NAME

Total Number:

Names of personnel receiving PHDs

NAME

Total Number:

Names of other research staff

NAME   PERCENT_SUPPORTED

FTE Equivalent:
Total Number:

Sub Contractors (DD882)

Inventions (DD882)

September 30th, 2009

Phase I Final Report

Development of III-Nitride Based THz Inter-Subband Lasers

Professor Manijeh Razeghi
Department of Electrical Engineering and Computer Science
Center for Quantum Devices (CQD)
Northwestern University
2225 N. Campus Drive, Cook Hall 4051, Evanston, IL 60208

Graduate Students:

Can Bayram

Erdem Cicek

Zahra Vashaei

Research Scientists:

Ryan McClintock

Nicolas Pere-Laperne

Paul Giedraitis

1

Abstract: (200 Words)

III-Nitrides, due to their large conduction band offset and fast transition speeds, are promising constituents for intersubband (ISB) devices. In addition, III-Nitrides are characterized by a very large phonon energy (90 meV). This makes them ideally suited to the realization of near room temperature operating THz lasers. The objective of this program has been to demonstrate the potential for using III-Nitrides to realize a room temperature operating terahertz intersubband laser.

As part of this contract, a comprehensive model of intersubband transitions was developed that takes into account the important effects of strain on bandstructure and piezo-as well as spontaneous- electric fields. Interband photoluminescence and intersubband absorption measurements were performed to help develop the modeling. We demonstrated the shortest MOCVD-grown III-Nitride intersubband absorption wavelength of 1.5 μm as well as the longest intersubband wavelengths of 5.3 μm, by any growth technique. In addition to investigating the optical properties we fabricated and tested both resonant tunneling diodes and quantum well infrared photodetectors in order to investigate quantum transport in III-Nitrides. Based on the refined III-Nitride intersubband models designs were also developed for room temperature terahertz emission via optical pumping. Electrical injection designs were also proposed for both polar and non-polar growth orientations.

Keywords:

<u>Outline</u>

1. Introduction & Summary

III-Nitrides, due to their large conduction band offset and fast transition speeds, are promising constituents for intersubband (ISB) devices. The first demonstration of intersubband transitions in this material system was grown by Molecular Beam Epitaxy (MBE). Later, MBE-grown material has shown ISB transitions (ISBTs) covering the 1-2 µm regime. In contrast, early attempts at Metalorganic Chemical Vapor Deposition (MOCVD) grown material had largely failed to demonstrate intersubband transitions in this regime. Thus on of our first goals was to develop the MOCVD growth of II-Nitride ISB devices. In this report, we demonstrate a new pulsing technique realized by MOCVD to show that MOCVD has the capability of achieving ISB transitions at 1.5 µm – the lowest ISBT wavelength ever achieved by MOCVD. Moreover, we have optimized high quality AlGaN/GaN SL and demonstrated ISB absorption as high as 5.3 µm – the highest ISBT wavelength ever achieved by MOCVD, MBE or any other growth technique. With these demonstrations, we have proven MOCVD as a reliable means of growing high quality III-Nitride ISB devices.

Before ISB transitions could be demonstrated, we first had to develop appropriate theory that includes effect of strain on bands and piezo-as well as spontaneous- electric fields. In this report, we present our recent progress on theory/simulation and experimental accomplishments. We also explain our research map to go from the mid-infrared range to the THz one. The goal of demonstrating a THz emission with a quantum cascade structure based on III-Nitride material is investigated with different methods. We are currently working on absorption and emission by optical pumping for a light-matter coupling. In the same time, we are working on transport and resonant tunneling in GaN/AlGaN material. This carrier transport is a key requirement to realize a good emitting structure. For the moment, the increase of the wavelength is proposed by different designs for the absorption and for the optical pumping.

Base upon our developed theory, we came up with a design for ISB absorption at 1.55 µm. However, achieving ISB transitions via MOCVD grown III-Nitride material required development of a new pulsing technique specifically designed targeting GaN/AlN superlattices. This unique pulsing technique enabled us to achieve high optical and structural quality SLs characterized by atomic force microscopy, scanning electron microscopy, photoluminescence, and X-ray diffraction.[1] After this world's first demonstration of ISB at 1.5 µm[2,3], we have developed the theory, and came up with a design for ISB absorption at 5.3 µm. Achieving ISB transitions in mid-infrared range required development high quality growth technique specifically designed targeting GaN/AlGaN superlattices. In conclusion, we have demonstrated ISB transitions from 1.5 to 5.3 µm for the first time in the world by MOCVD.[4]

This report is composed of two main parts. The simulation & design section concentrates on our primary designs. This section tries to show how we interpret the experimental results

and in the same time give some designs and propositions for the next stage of emission in particular. The second main part, concentrates on the actual results obtained with high quality material grown by MOCVD. These results are for the moment focused on absorption measurements. At the end a future work section summarizes our plans for moving forward and realizing ISB lasers.

2. Simulation and Design

Realizing a THz quantum cascade laser based on III-Nitride multi-quantum-well structure requires understanding both the material characteristics as well as the device performance factors. A complete theory and simulation background is thus necessary to develop device designs and understand the material system of GaN/AlGaN. A quantum cascade laser is composed of three different steps, the injection, the emission and the extraction. Each step is independent physics-wise, and requires extensive study to realize an optimum design. However, they can be treated separately before integration into the final laser structure. The emission is studied by both absorption measurements and optical pumping measurements. To study the injection and tunneling, we are developing a resonant tunneling diode (RTD). In this section, we present the different device designs we are developing to help demonstrate the three different steps of a QCL, the injection, the emission, and the extraction. At this time, this work is largely targeting an intermediate wavelength. However the experience, technological development, and other skills we are developing in this work, are applicable to longer wavelengths. Once a solid basis is developed we will work on extending our results towards THz regime. In this section we explain the current status of our work and our approach for reaching the THz regime.

2.1. Intersubband Absorption

Intersubband absorption measurement is a primary means to demonstrate intersubband optical transitions in our GaN/AlGaN material.[5] This experiment is a first step to precisely know if our material quality and superlattice interfaces are good enough to form intersubband levels.

In order to measure the intersubband absorption we send a broad spectral range source (black body) towards the multi quantum well structure and collect the light from the other end. Using a FTIR we can collect the spectrum of the light transmitted through the sample, normalizing to the background spectrum we can determine the absorption. Using s- or p-polarized light, the absorption thanks to the MQW intersubbands are identified. The absorbed light energy should correspond to the energy between the two confined electronic states of the well. As a consequence, we should see the intersubband absorption via this transmission experiment. A more detailed description of the measurements are included in the experimental section (Section 3.7).

This experimental step is crucial to validate our simulation/design as well as the material quality. As a consequence, this primary experiment will have to be done for each aluminum

content studied. However, moving straight to THz is difficult due to absorption of Sapphire at THz wavelengths requiring substrate removal (discussed more in Section 3.1)

2.1.1 Intersubband Absorption at Short Wavelengths (1-2 μm)

The aluminum content of the first structure we studied corresponds to a GaN well and AlN barrier (i.e. a binary-binary superlattice). This material has been chosen for the high capability in CQD to grow such material by MOCVD. This first experiment serves as an initial demonstration to validate our approach to reach longer wavelength and move into the THz range.

The band offset between AlN and GaN is E_{offset} = 1.75eV. In absence of an external electrical field and of any deformation due to stress, the hexagonal wurtzite phase exhibits (polarization along the [0001] axis) so called spontaneous polarization (P_{sp}). Simply because at the microscopic scale, the centers of gravity of charges of opposite signs are not in the center of the bound. In addition, due to the lattice mismatch (2.4%) between the superlattice layers, a piezoelectric polarization appears in GaN/AlN multi quantum well structure. It is necessary to take both of these effects into account in our simulations. Our simulation achives this via the introduction of an internal electric field applied to the wells and to the barriers. Figure 1 presents the conduction band of a superlattice with 17 Å GaN wells and 30 Å AlN barriers. This multi quantum well structure's band profile shows the significant effect of this internal electric field creating a triangular shape to the wells. In this figure, we represent the square moduli of the wavefunctions of the multi quantum well structure. We find out two bound states in the quantum well separated by ΔE = 830meV. The vertical red arrows correspond to the intersubband absorption. Experimental results are described in Section 3.7.
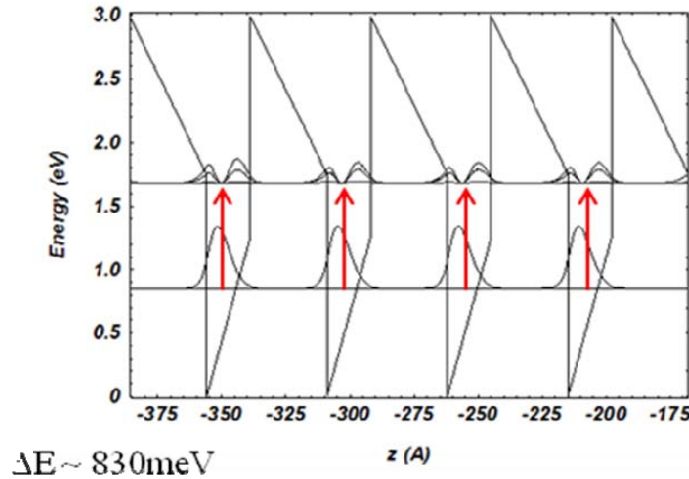
Figure 1: Band diagram of a muti-quantum well structure consisting of 17 Å thick GaN wells and 30 Å thick AlN barriers.

2.1.2 Intersubband Absorption at Longer Wavelengths (3-6 µm)

With GaN/AlN material, the absorption limitation is about $\lambda = 2.5$ µm. In order to reach longer wavelength and consequently to reach THz (30-200µm), we need to change the aluminum content of the barrier.[6] Indeed, decreasing the aluminum content leads to decrease the well/barrier band offset. For example, with a 33% aluminum content the band offset is $E_{offset} = 0.58$eV. Figure 2 presents the band diagram of a a multi quantum well structure with 20 Å GaN wells and 40 Å $Al_{0.33}Ga_{0.67}N$ barriers. Two bound states are present in each quantum well separated by an energy of $\Delta E = 410$meV, which corresponds to an intersubband absorption at 3 µm. This structure is an important step in our research project because we are switching from GaN/AlN to GaN/AlGaN. Going from binary-binary to binary-ternary interfaces complicates the growth. The growth quality needs to be optimized to obtain a good quality GaN/AlGaN multi-quantum well material.
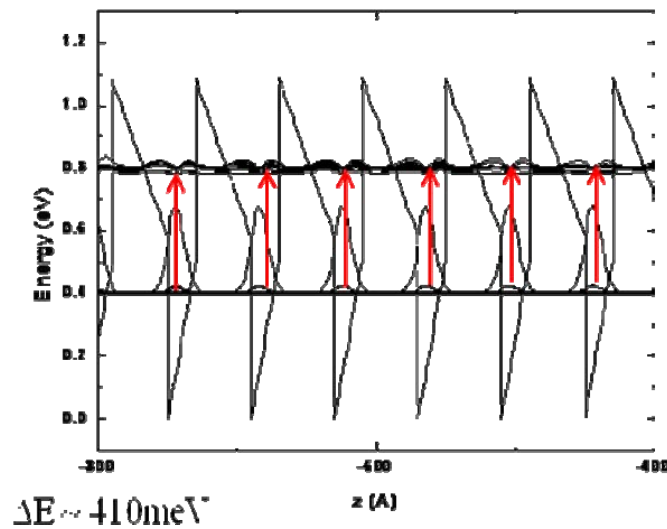
Figure 2: Band diagram of a multi quantum well structure with well in GaN of 20 Å and barriers in $Al_{0.33}Ga_{0.67}N$ of 40 Å.

With such an aluminum content, we can design structures in the mid-infrared range, 3-6µm. For longer wavelength, we need to decrease again the aluminum content further. The development of lower aluminum content AlGaN/GaN superlattice is currently in progress, and the preliminary results are discussed in the experimental section (Section 3.5).

In parallel to these absorption measurements, we are also developing other experiments to observe intersubband emission, rather than absorption, of light. This approach is presented in Section 2.4.

2.2. Photoluminescence

Photoluminescence (PL) is a powerful tool to characterize a multi quantum well structure. This experiment allows us to determine the difference in energy between the

confined states in the conduction and valence bands. In the experimental section (Sub-Section 3.4.5), we present additional PL results obtained for our GaN/AlN structures.

Photoluminescence is largely an inter band phenomena, as such in order to understand he PL it is necessary to also model the behavior of the valence band. We performed simulations of the PL energy calculating the confined energy of the heavy hole in the valence band and the first electronic confined state in the conduction band.
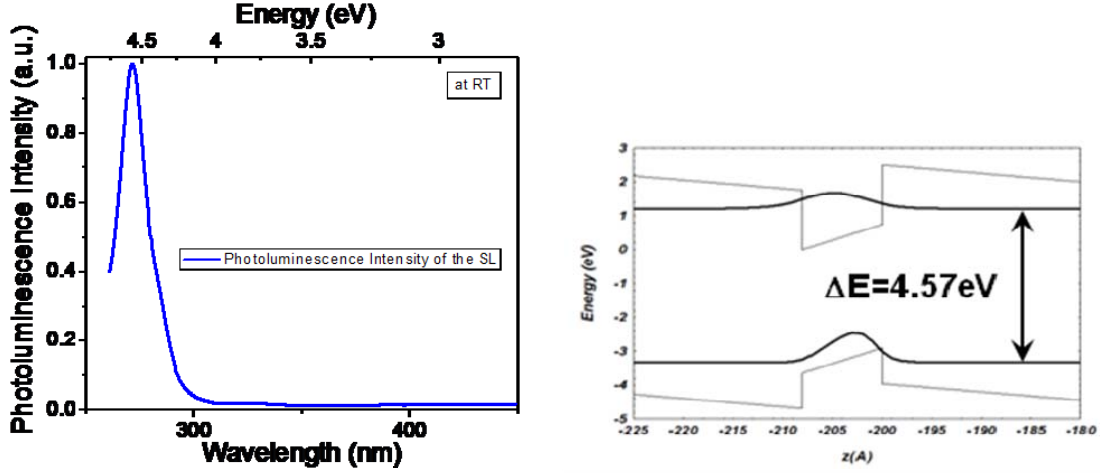
Figure 3: Photoluminescence spectra of 7.5 Å GaN well and 30 Å AlN barrier multiquatum well structure. Simulation of a 7.5 Å GaN well and 30 Å AlN barriers

Figure 3 above shows the good agreement between theory and experiment. The experimental PL energy is located at 4.51eV and the calculated one is 4.57eV. The small difference of only 60 meV is attributed to the uncertainty of the well and barrier widths.

For samples with different capping layers (see Sub-Section 3.4.5), we found an increasing wavelength PL peak intensity by increasing the cap layer thickness. With increasing capping layer thickness, the peak position also blue-shifts. Structurally, the sample also becomes more cracked with thicker AlN capping due to strain-relief mechanism. We are currently trying to interpret this blue-shift by an effect of strain reduction due to crack formation..

In conclusion, PL measurement can be a useful tool to characterize the confinement and the design of the quantum well structure, but in the same time, we may evaluate the strain between the GaN and AlN layers in our superlattice.[7] We have realized a reliable theory/simulation to correlate the experimental PL results with the theoretical calculations.

2.3. Polar vs. Non-Polar Growth Orientations

As discussed above, the large spontaneous and piezoelectric polarizations inherent in polar *c*-plane growth have a significant effect on the resulting band structure. The use of different growth planes for the intersubband experiments has been proposed since the beginning of the studies on GaN/AlGaN material. The fabrication of high-quality nitride

epitaxial layers, grown in either (0001) *c*- or, more recently, non-polar {11$\bar{2}$0} *a*- and {1$\bar{1}$00} m-plane directions (Figure 4) using either GaN templates, free-standing GaN substrates, and/or LiAlO$_2$ substrates have been reported.[8]

The growth orientation has strong electronic implications when it comes to nitride superlattices and quantum wells. The intrinsic property of GaN-based structures grown along the main symmetry direction *c*-plane is a large electric field induced by piezoelectric and spontaneous polarization, which significantly alters the conduction band profile (as presented in the absorption section, Section 2.1). On the other hand, the non-polar *m*- and *a*-plane orientations of the crystal cancel the spontaneous polarization and therefore considerably lower the intrinsic electric field strength, making the design less sensitive to variations of the polarization fields. Another advantage of using a non polar growth orientation could be decreased tunneling across the barriers – one consequence of the high electric fields could be the increase of the tunneling mechanisms across the barriers, which may have a negative impact on intersubband emitters.[9]
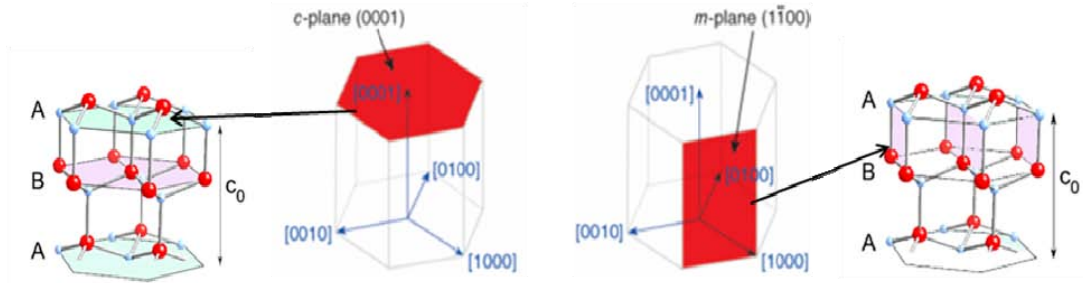
Figure 4: Crystallographic structure of GaN and AlN. Sketch of the crystallographic plane.

Several groups have demonstrated that GaN-based quantum wells grown on the nonpolar m- and a-planes exhibit photoluminescence characteristics that are consistent with a lack of polarization-induced electric fields. The emission wavelength from an *m*-plane heterostructure was blue-shifted relative to the comparable structure grown on *c*-plane GaN. Furthermore, the radiative lifetimes in the *m*-plane structure were one to two orders of magnitude shorter than for the *c*-plane structure.

We performed simulations in both cases, one taking into account the internal electric field due to the spontaneous and piezoelectric effects and another one without any internal electric field. A comparison of the two structures is shown below in Figure 5.
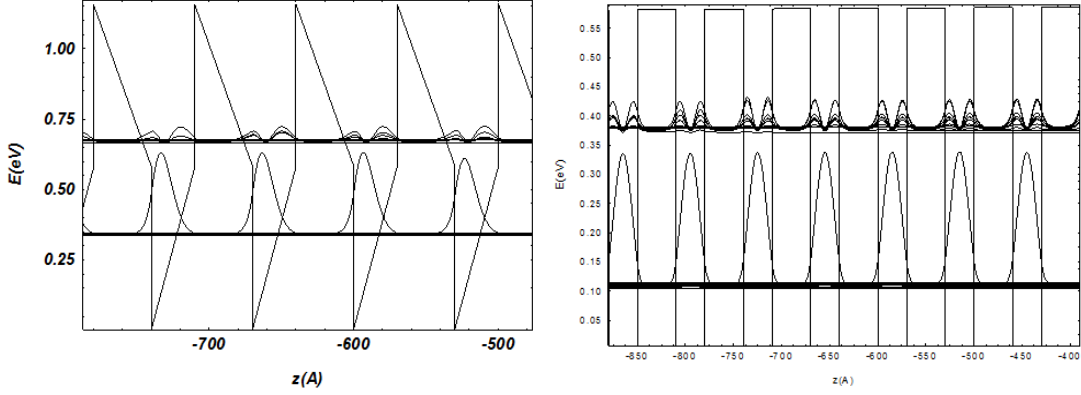
Figure 5: Band diagram and square moduli of the wavefunctions for a 30 Å GaN well and 40 Å Al$_{0.33}$Ga$_{0.67}$N multiquantum well structure with (without) the effect of internal electric field on left (on right).

In Figure 5, the interest in growing on a non-polar plane is clearly demonstrated. First, the effective barrier width for the second level in the quantum well is thinner in the case of multi quantum wells grown on a *c*-plane than on plane without internal electric field. As a consequence, the confinement potential for the high lying energy levels is reduced due to tunneling through the triangular barriers due to the internal electric field. Secondly is negative argument of *c*-plane growth: as represented in Figure 5, the wavefunctions are distorted in presence of an internal electric field. The shape of the wavefunctions is not symmetric anymore regarding the center of the quantum well. As a consequence, the optical dipole matrix element of the intersubband transition is decreased and leads to a lower optical coupling. To finish with, the last argument in favor of *a*- and *m*-plane growth concerns the ability to design structures with an important number of quantum wells. In conventional THz quantum cascade laser, one period is composed of at least four quantum wells, however the design can be much more complicated in order to obtain the best injection and extraction which lead to high performance lasing effect.

In the experimental/growth section, we develop our current research status for these different growth planes.

2.4. Optical pumping experiments

We have already started a theoretical study to design an optically pumped structure. This experiment should be the first demonstration of an intersubband emission with a GaN/AlN structure. In a similar approach as for the absorption, we are using a GaN well and AlN barrier to growth availability (this may change as the AlGaN/GaN structures are optimized). As a first step, we expect to observe spontaneous emission, after which a stimulated emission. Due to the GaN/AlN SL materials used, we expect to design a structure emitting in the near-infrared region, in order to demonstrate our capability to observe an intersubband emission and validate our experimental set-up.

The principal of optical pumping is bringing electrons into the upper electronic subband via absorption of light from an external laser source. The excited electron, on an upper subband, is expected to relax in a lower subband radiatively. To realize the optical pumping experiments in an intersubband structure, there are two methods. First is to pump the electron from the valence band to the conduction band, that is to say an interband pumping, in our material with a Cadmium vapor laser whose wavelength is around 3.6 eV. Second method is to use a laser with a wavelength fitted for an intersubband pumping from a subband in the conduction band to another subband in the same band. In the section, we will discuss the best way to follow via quantum efficiency.

### 2.4.1 Design of different structures

Figure 6 represents the first design proposed for an intersubband emission with GaN/AlN material by optical pumping of the subband levels. In this figure, we represent a vertical straight arrow which corresponds to the intersubband pumping process for subband 2 to subband 9. Emission is designed to occur between subbands 9 and 7, which leads to an emission around 1.65µm. After emission, electrons are extracted from this lower level by a primary cascade. For the moment, the extraction is not fully studied. In this configuration, for the intersubband pumping, we need to use a YAG laser (pump around 1.12 µm).
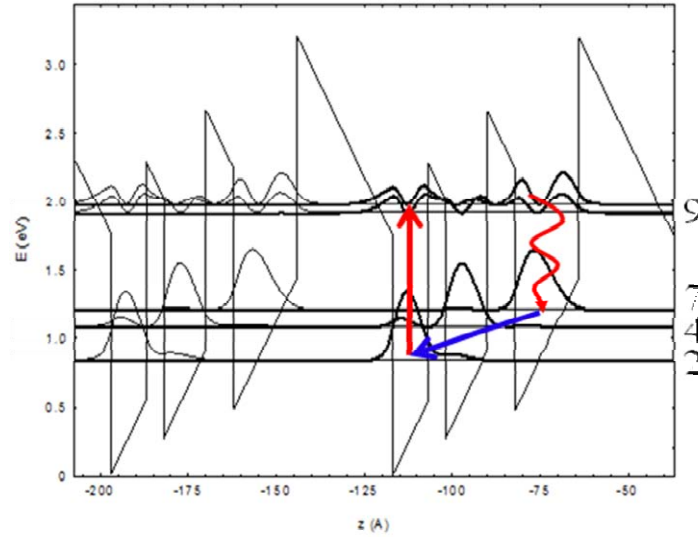
Figure 6: Optical pumping design emitting at 1.65µm. We represent the conduction band and the square moduli of the wavefunctions, the red straight arrow corresponds to the intersubband pumping from subband 2 to 9, the wavy arrow stands for the radiative emission and the blue arrows corresponds to the extraction of carriers from the lower subband.

The second structure, we have designed, is made of barriers with a lower aluminum content, designed for longer wavelength emission. In order to reach longer wavelength we are using $Al_{0.33}Ga_{0.67}N$ barriers and GaN wells.
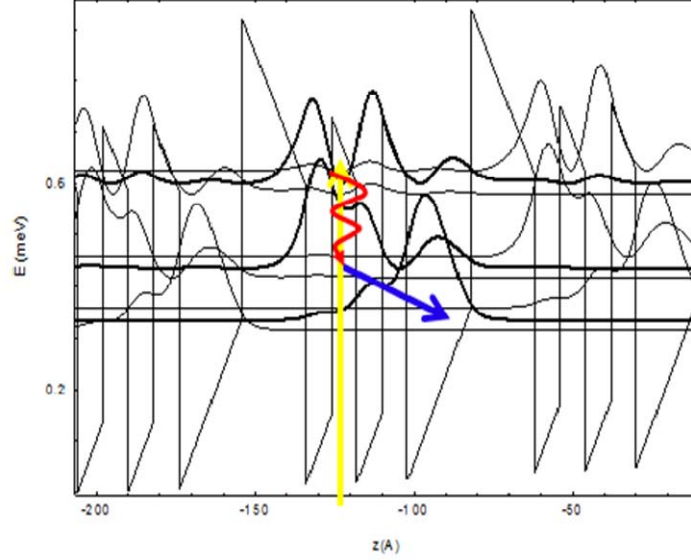
Figure 7 : Optical pumping design emitting at 7 µm. We represent the conduction band and the square moduli of the wavefunctions, the yellow straight arrow corresponds to the interband pumping from the valence band to a subband of the conduction one, the wavy arrow stands for the radiative emission and the blue arrows corresponds to the extraction of carriers from the lower subband.

As in the absorption experiment, changing the aluminum content leads to a different band offset between the barriers and the wells. Figure 7 represents the conduction band of the multi quantum well structure and the square moduli of the wave function. Pumping is expected to occur from the valence band to the upper subband in the conduction band. Emission occurs between two subband spaced in energy of 170meV which corresponds to 7µm. The extraction is achieved by emission of LO-phonon. This design is still under progress especially to reach different wavelengths with the same aluminum content. The pumping part is not optimized yet.

2.4.2 Quantum efficiency

The quantum efficiency is defined for such an experiment by the following expression[10]:

$$\eta = a \frac{\lambda_p}{\lambda_e} \frac{\tau_9}{\tau_{97}^{rad}}$$

where a is the absorption coefficient in the multipass waveguide, λ_p the wavelength of the pump, λ_e the wavelength of emission, τ_3 the lifetime of the upper level of the radiative transition and τ_{32}^{rad} the radiative lifetime transition, reported to be 27 ns.

Using this expression, we first observe that the quantum efficiency is directly linked to both wavelengths of pump and emission. Obviously, the pump wavelength has to be higher than the emitted one, but the closer it is, the higher the quantum efficiency. So preferably, we

would want to use intersubband pumping compared to the interband one. Intersubband pumping also avoids over-filling the lower subbands

For the first design, targeted to emit at 1.65 µm, the quantum efficiency is calculated. We determine the scattering lifetime of subband involved in the radiative transition. We assume, in a first approximation, the main scattering process is the emission of LO-phonon from the upper level to the lower ones. We calculate the scattering time thanks to this expression[11]:

$$\frac{1}{\tau_i} = \frac{m^* e^2 \omega_{LO}}{2\hbar^2 \varepsilon_p} \sum_f \int_0^{2\pi} d\theta \frac{\int dz \int dz' \chi_i(z) \chi_f(z) e^{-Q|z-z'|} \chi_i(z') \chi_f(z')}{Q}$$

$$\text{where} \quad Q = (k_i^2 + k_f^2 - 2k_i k_f \cos\theta)^{1/2}$$

$$\text{With } k_f^2 = k_i^2 + \frac{2m^*}{\hbar^2}(\varepsilon_i - \varepsilon_f - \hbar\omega_{LO})$$

The results are in the following table:

$1/\tau_{i\text{-}j}$ (s^{-1})	9-7	9-4	9-2	7-4	7-2
LO phonon scattering	4.5 10^{12}	2.4 10^{12}	5.8 10^{10}	7.7 10^{12}	2.6 10^{11}

Table 1: Scattering time for from subband i to subband j by emission of LO-phonon

Thanks to these results, for the particular structure presented in Figure 6, we find a quantum efficiency of $\eta = 0.35\mu$W/W.

2.4.3 Experimental set-up

This experiment has never been realized in the CQD. As a consequence, we need to build a setup and adapt it to the intersubband specificities. For the intersubband pumping, we need to send the light into one facet of the sample and collect the emitted light from the other facet.
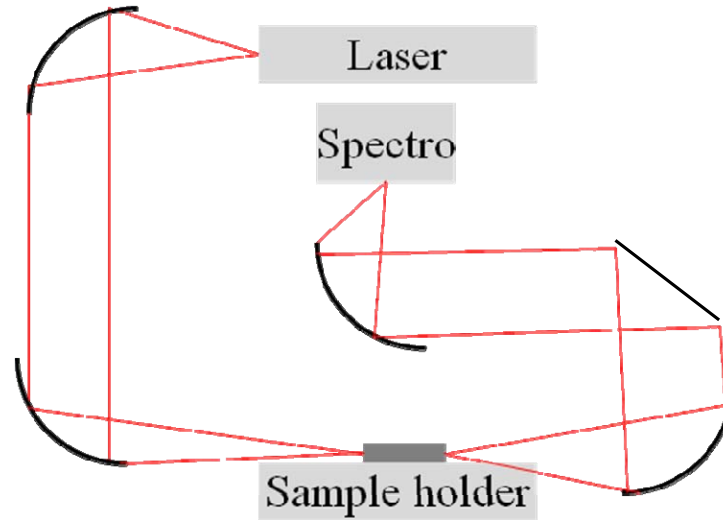
***Figure 8 : Sketch of the optical pumping set-up for an intersubband pump and intersubband emission***

The design of this setup is still under consideration, however a preliminary layout is shown above in Figure 8. We plan to make this experiment at low temperature in order to remove most of the thermal excitation, so we are in the process of buying a new cryostat with appropriate windows. This requires the windows be a close as possible to the sample, and that they be suitable for THz transmission as we move to longer wavelengths.

Processing of such a device has still to be clarified. We may form cavities as in other semiconductor lasers.

2.5. Resonant tunneling diode (RTD)

The realization of a resonant tunneling diode is an important experiment to provide evidence for the transport in a quantum structure. This point has to be demonstrated and studied with GaN/AlGaN material because it is a key parameter for the realization of a quantum cascade laser in GaN/AlGaN. It is actually resonant tunneling which allows the QCL stages to be chained together and allows injection of carriers into upper subband.

The principle of a resonant tunneling diode is depicted in Figure 9 below. A resonant tunneling diode corresponds to one quantum well between two heavily doped layers. When an electric field is applied, the current flowing through the structure increases to reach a peak (I_{peak}). In a second step, there is a negative differential resistance to reach a current I_{valley}. The observation of this peak and valley current is the main experimental evidence for the resonant tunneling occurring in the diode.
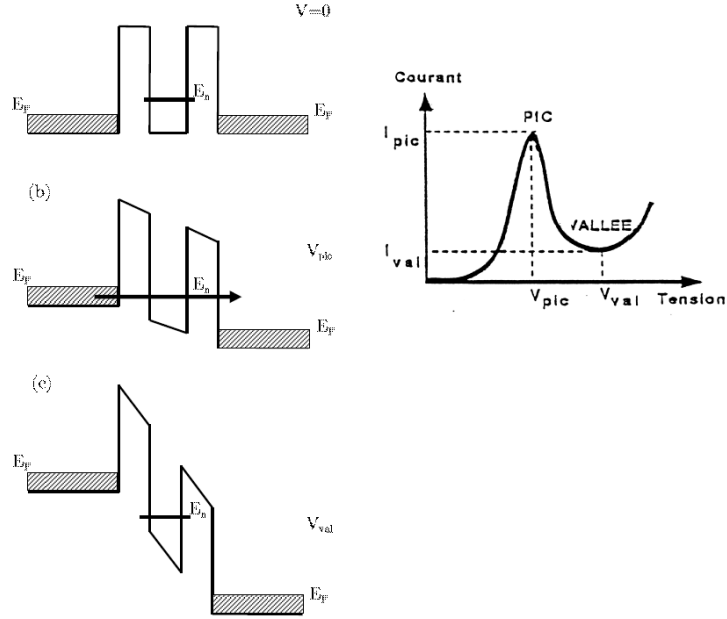
Figure 9 : Sketch of a resonant tunneling diode under different electric field

2.5.1 RTD Design

We took a reported design made out of GaN/AlN[12], with 300nm GaN Si doped $5x10^{18}cm^{-3}$, 10Å AlN / 7.5Å GaN undoped / 10Å AlN 500nm GaN Si doped $5x10^{18}cm^{-3}$ on an AlN buffer layer and on sapphire.
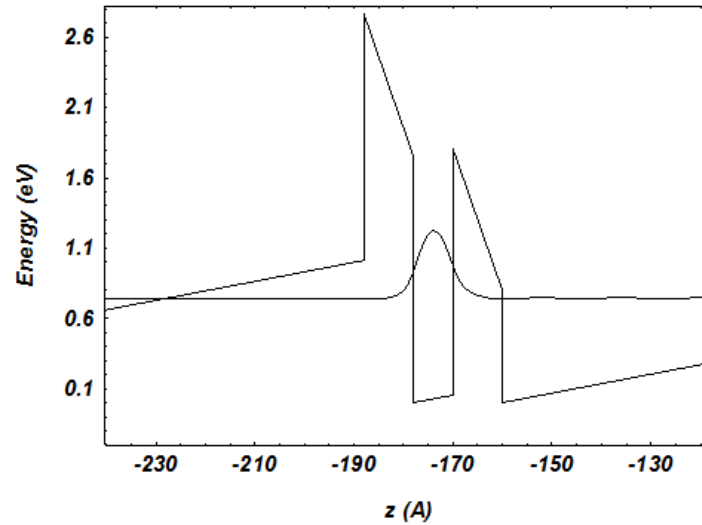

Figure 10: Band structure of an RTD and the square moduli of the wave function for a 300nm GaN Si doped $5x10^{18}cm^{-3}$, 10Å AlN / 7.5Å GaN undoped / 10Å AlN 500nm GaN Si doped $5x10^{18}cm^{-3}$ on an AlN buffer layer and on sapphire.

Figure 10 represents the conduction band of the resonant tunneling diode and the square moduli of the wavefunction. This figure just represents the quantum well confinement and does not take into account the doping level in the contact layers. We need to develop a self consistent Schrödinger-Poisson simulation to be able to entirely calculate this structure. This program is the main part of our future work for the simulation section.

2.5.2 Realization of the RTD

Our first attempt to realize a RTD was using a GaN/AlN material due to the growth maturity of it in CQD. This design is made of thin AlN barriers and a 7.5Å thick GaN well. The sharpness of the interfaces between the two materials is a key parameter for the success of this experiment. As presented in Figure 11, the first growth presented a high surface roughness (9 Å) after the growth of the active layer. This value is higher than the well width, so we have serious doubt about the presence of quantum well in this structure. As such, the first results are inconclusive. Soon, we will redo the experiment. In the same time, we will focus our attention on lower aluminum content barrier RTDs. Lower barriers has the advantage of reducing the strain between the wells and barriers making it easier to realize better interface for such thin layers.
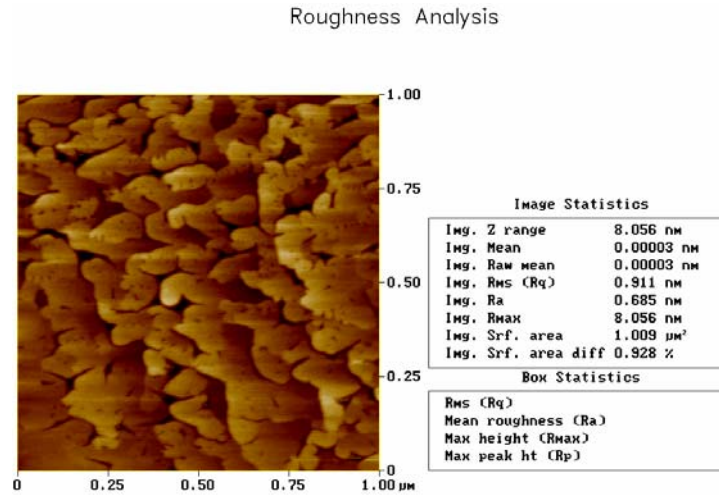
Figure 11 : Roughness analysis for the RTD sample after the active region growth (10Å AlN / 7.5Å GaN undoped / 10Å AlN 500nm GaN Si doped 5x10^{18}cm^{-3} on an AlN buffer layer and on sapphire)

2.6. Conclusion

In conclusion, we are developing different experiments to realize a THz quantum cascade structure. We are validating our approach and our material by measuring the intersubband absorption for different aluminum contents. At the same time, we are developing a new experiment to observe an intersubband emission in a nitride structure by optical pumping. And finally, resonant tunneling in order to successfully demonstrate injection for a quantum cascade laser will be investigated via RTD development.

Concerning the simulation and design part, we have to improve our model by coupling the Schrödinger and Poisson equations in order to take into account the doping effect in our structure. This improvement is necessary not only for the absorption measurement but also for the optical pumping structures. We need to develop and simulate more designs to emit from the near infrared range to the far infrared one.

In a near future, we need to design and develop electrical pumping structure for the emission with different aluminum content and finally find the best one, in terms of material quality to reach the THz range.

3. <u>Experimental approach</u>

A pulsed metal-organic chemical vapor deposition technique has been developed for the growth of high quality AlN/GaN superlattices (SL) with intersubband transitions at optical communications wavelengths. The tunability of the AlN and GaN layers thickness is demonstrated. Indium is also shown to act as a surfactant and help improve the SL surface and structural quality. Using this technique, we have grown a variety of different superlattice structures for intersubband absorption. We have also investigated the effects of capping this superlattice. The superlattice capping layer thickness is shown to be crucial for intersubband (ISB) transition characteristics. We have also studied the effects of barrier- and well-doping on the ISB absorption.

3.1. Substrate Investigation: Transmission of Sapphire and SiC templates

In the near infrared range, the template consists of a high-quality AlN layer grown on double-side polished (001) sapphire substrate. We have investigated the absorption of our template using a Fourier transform infrared spectrometer. In performing this investigation a strong absorption was notices at the wavelengths of interest. This absorption was deduced to arise form the sapphire substrate. Figure 12 represents the transmission spectrum of a sapphire substrate in the range 1 µm to 27 µm. The light is observed to be totally observed in the range from 7.5 µm to 26µm. As a consequence, the use of sapphire substrates is not suitable for a continuous study from near-infrared to the THz range. Additionally since effective optical wave-guiding at THz wavelengths is difficult to achieve with out the use of metal waveguides, the substrate will become past of the laser cavity. Thus, if sapphire is used as a substrate, it will be necessary to completely remove the substrate during the processing (discussed in more detail in Section 0).

However, we have studied another substrate material suitable for the GaN/AlGaN growth – 6H-SiC. We used the same technique to measure the transmission in the range 1µm to 60µm. This material absorbs in a windows from 6µm to 14µm. For the same reason as for Sapphire, this substrate is not suitable for a continuous study (increasing continuously the wavelength) as described in the simulation section. However, it may prove promising at THz wavelengths.
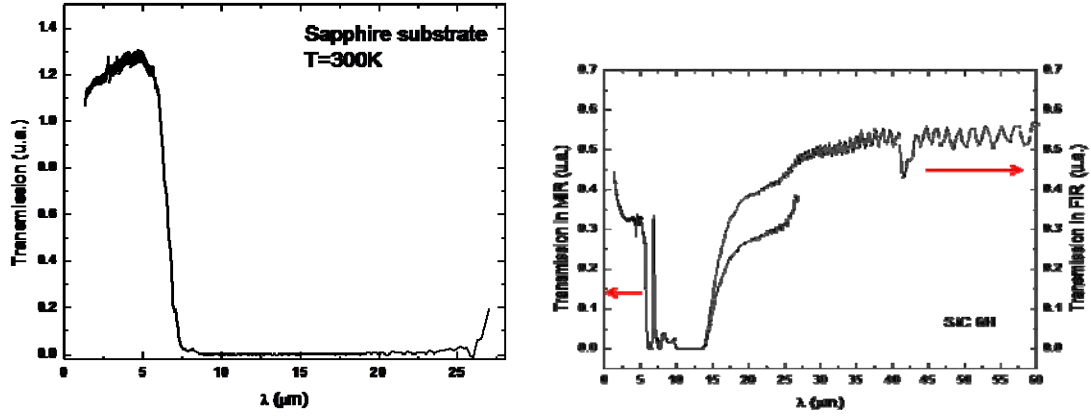
Figure 12: Transmission spectra of a sapphire substrate from 1µm to 27µm. Transmission spectra of a SiC substrate from 1µm to 60µm.

Due to the substrate issues, and the desire to investigate non-polar device designs, we have decided to purchase GaN substrates. We have ordered *c*-, a-, and m-plane GaN substrates from Kyma Tech. The substrates were recently received and growth optimizations are in progress. Meanwhile, we are improving the active layer growths on *c*-plane sapphire substrates.

3.2. Growth of Very High Quality AlN/Sapphire Templates

We have developed a novel pulsing technique to realize high quality AlN on sapphire. Optimization of the low temperature buffer layer is realized in harmony with the pulsing parameters (such as deposition times and flow rates).
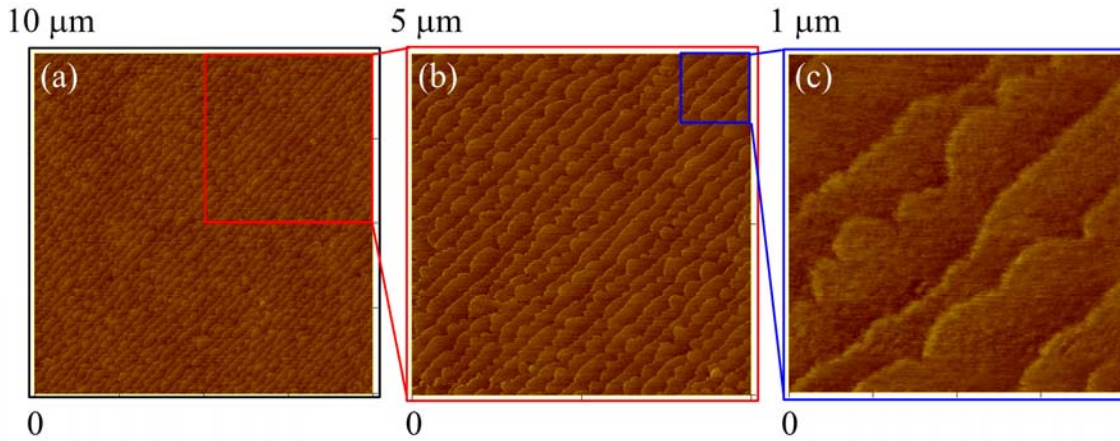

Figure 13: AFM images of high quality AlN grown on sapphire. (a) (10 µm x 10 µm), (b) (5 µm x 5 µm), and (c) (1 µm x 1 µm) areas have root mean square (RMS) roughness of 1.38, 1.33 and 1.35 Å, respectively

Figure 13 shows the AFM images of high quality AlN grown by our pulsing technique. The root-mean-square (RMS) of (10 µm ×10 µm), (5 µm ×5 µm), and (1 µm ×1 µm) is 1.38,

19

1.33, and 1.35 Å, respectively. The atomic steps and their clear parallel orientation are seen in Figure 13 that demonstrates the atomic smoothness.

Photoluminescence and X-ray diffraction studies are realized, and shown in Figure 14. Inset shows the symmetric (002) (full-width-at-half-maximum (FWHM) of 40 arcsec) and asymmetric (105) (FWHM of 142 arcsec) omega/2theta scan of the AlN/sapphire template. These values are the state-of-the art results that enabled us to achieve high quality materials.
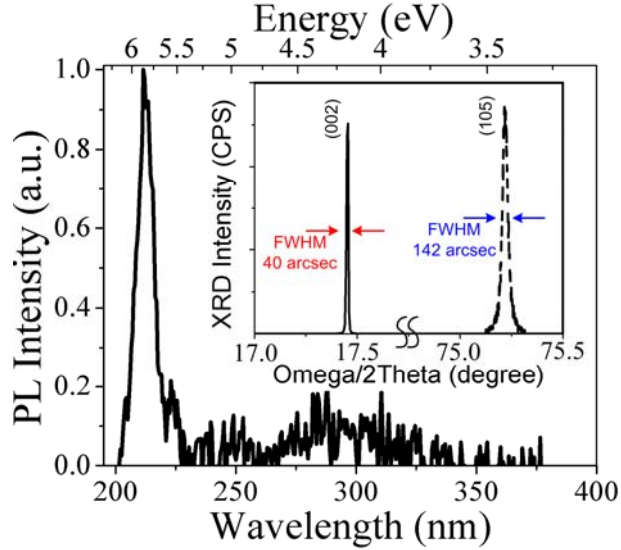
Figure 14: Room temperature normalized photoluminescence of high quality AlN/sapphire template. Inset shows the symmetric (002) (full-width-at-half-maximum (FWHM) of 40 arcsec) and asymmetric (105) (FWHM of 142 arcsec) omega/2theta scan of the AlN/sapphire template.
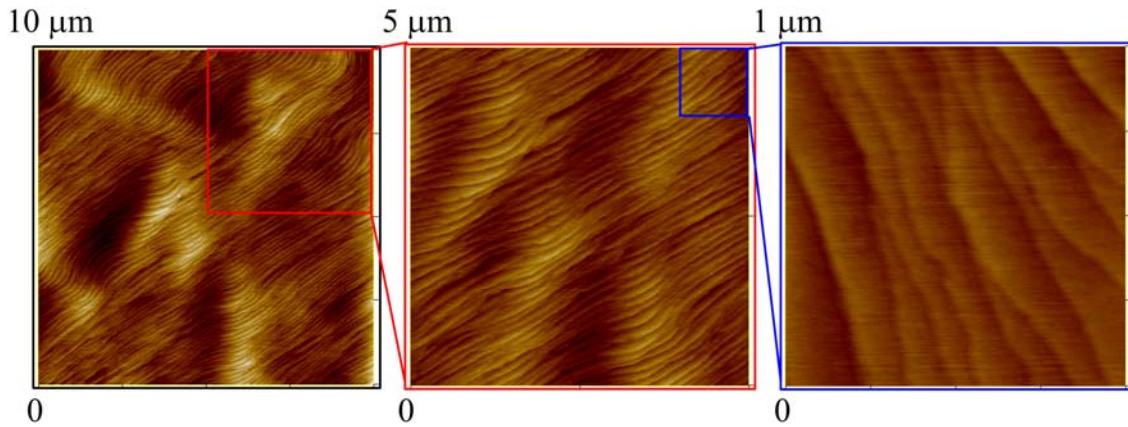
3.3. Regrowth of Very High Quality GaN on AlN/Sapphire Templates

We have realized high quality GaN regrowth on our novel AlN/Sapphire templates. For the sake of comparison, GaN samples were grown on AlN/LT-AlN buffer/sapphire templates and directly on LT-GaN buffer/sapphire substrates. Table 1 shows the electrical and structural properties of GaN layers deposited on both templates. Higher mobility and lower X-ray full-width-at-half-maximum (FWHM) indicates the superior quality of GaN on AlN/LT-AlN buffer/sapphire templates over on LT-GaN buffer/sapphire ones.[13] Atomic force microscopy (AFM) also demonstrates much smoother surface with clear evidence of atomic steps for GaN/AlN/sapphire (Figure 15).

Table 1: Properties of unintentionally doped GaN on LT-GaN buffer/sapphire and AlN/LT-AlN buffer/sapphire.

Unintentionally doped GaN on	Background Carr. Conc. (cm^{-3})	Mobility (cm^2/V·s)	(002) FWHM (arcsec)	RMS Surface Roughness (Å)
LT-GaN buffer/sapphire	-1.95×10^{17}	188	380	2.14
AlN/LT-AlN buffer/sapphire	-4.25×10^{16}	541	220	1.74

Figure 15: AFM images of high quality GaN grown on AlN/sapphire. (a) (10 µm x 10 µm), (b) (5 µm x 5 µm), and (c) (1 µm x 1 µm) areas have root mean square (RMS) roughness of 3.47, 2.44 and 1.27 Å, respectively.

## 3.4. Growth of AlN/GaN Superlattices

Molecular beam epitaxy has been successfully used to realize intersubband AlN/GaN SLs absorbing at optical communications wavelengths. However, there are very few reports of intersubband absorption in metalorganic chemical vapor deposition (MOCVD) grown AlN/GaN SLs, especially in the in near-infrared, and even fewer leading to absorption lower than 2 µm. Today, most nitride based commercial optoelectronic devices are grown by MOCVD, and that is the growth technique available to us to complete this project. Thus, there is a wide interest to realize high quality ISB absorption by MOCVD.

3.4.1 Overview of the Pulsed Growth Technique

AlN/GaN SL, despite the lattice mismatch of 2.4%, can be realized crack-free and be grown pseudomorphically.[14] However III-Nitrides are piezoelectric materials, in conventional c-plane growth; these highly strained layers generate multi-MV/cm electric fields.[15] Thus, interface or SL thickness fluctuations degrade the absorption quality significantly.[15] Another problem is AlN/GaN or GaN/AlN interface stability, and their dependence on (GaN or AlN) template.[16,17] Moreover, the embedded GaN layer gets thinner during subsequent AlN

growth.[18,19] All these observations necessitate further MOCVD growth studies. To overcome the limitations of MOCVD growth, we propose and analyze a novel pulsed deposition technique for realizing AlN/GaN SLs, and demonstrate ISB absorption at telecommunication wavelengths.

Using conventional MOCVD growth, parasitic pre-reactions [20] between the TMAl and NH_3 necessitate lower pressures and smaller V/III ratios. The lack of aluminum adatom mobility also urges higher growth temperatures for AlN growth. In contrast, GaN typically obtains higher quality when grown under higher pressures and larger V/III ratios with moderate temperatures. The challenge in realizing high-quality SLs for ISB transitions is to find growth conditions that work simultaneously for both of these materials and yield well defined interfaces. One way to deposit GaN with a high V/III ratio while decreasing the parasitic pre-reactions when depositing AlN, is to use temporal separation of TMAl and NH_3 (or pulsing). This enhances the surface adatom migration of both the GaN and AlN and maximizes the growth efficiency.[21]
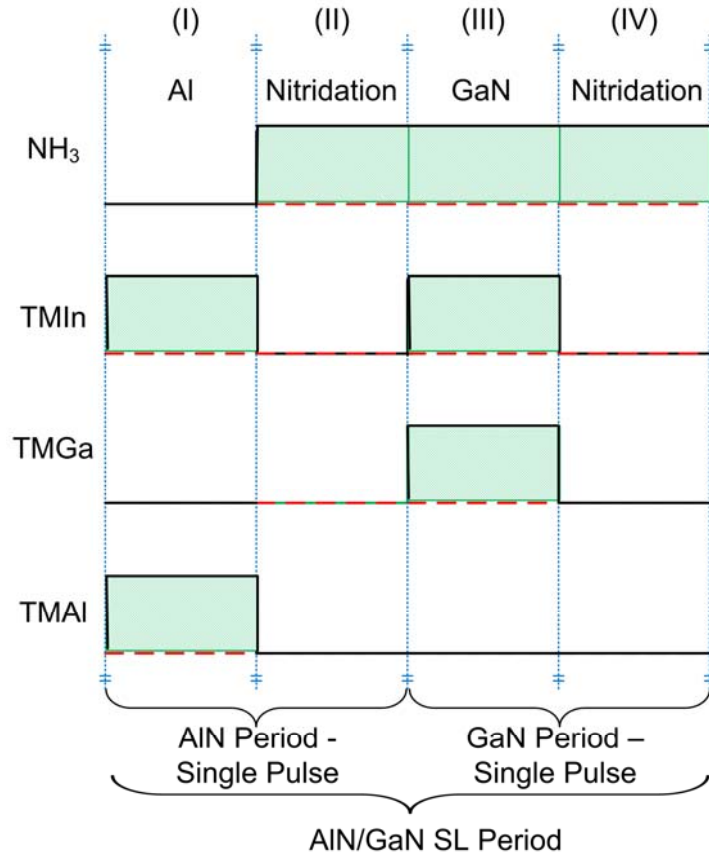

Figure 16: The growth sequence of AlN/GaN SL. One period consists of two main deposition phases: (1) AlN deposition, which is realized via pulsing TMAl and NH_3 to enhance aluminum adatom mobility (steps (I) and (II)), and (2) conventional GaN deposition (step (III)), which is realized by conventionally supplying TMGa and NH_3 simultaneously. Step IV nitridizes the surface.[1, 2]

The proposed SL deposition technique has two stages AlN grows, and GaN growth which each consist of two different steps for a total of four different steps as shown in Figure 16: Steps (I) and (II) result in AlN deposition, and may be repeated several times to obtain thicker AlN layers. The separate introduction of the group III and V precursors into the growth chamber in an alternating sequence enhances the diffusion length of aluminum adatoms leading to higher quality material. Step (III) deposits GaN using conventional bulk deposition to ensure a high V/III ratio. Step (IV) nitridizes the surface before aluminum deposition for the next SL period. This step prepares the surface for AlN regrowth by eliminating the excess gallium on the interface that may otherwise form an AlGaN interlayer, thus degrading the interface sharpness. Thicker GaN layers may be realized by either varying the length of the bulk-like growth step (Step (III)) or by repeating steps (III) and (IV). By using this pulsed SL deposition technique, the V/III ratio for AlN is decreased whereas that of GaN is maximized. This allows for a much higher AlN growth rate and aluminum adatom mobility than would be achieved with conventional growth. A typical sketch of the SL is given in the inset of Figure 18(a).

3.4.2 Effects of Indium on the SL Quality

In order to further enhance the adatom mobility and realize high-quality SLs, the use of indium (as a non-incorporating surfactant) is investigated. TMIn, is supplied along with TMAl and TMGa, as shown in Figure 16, to increase the mobility of the aluminum and gallium adatoms.
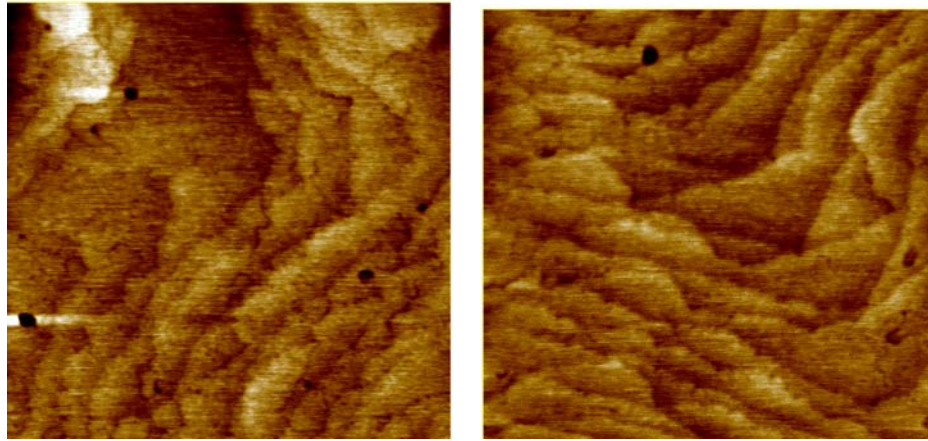

Figure 17. Left) the (1μm × 1μm) AFM of the SL surface without TMIn, Right) the (1μm × 1μm) AFM of the SL surface with TMIn.

Figure 17 show the atomic force microscopy (AFM) images of the surface of a SL grown without and with TMIn flow, respectively. The (1μm × 1μm) root-mean-square roughness decreased from 1.6 to 1.2 Å with the introduction of an indium surfactant. The dark spots in the AFM, corresponding to surface termination of screw-type dislocations, also decreased. In order to assess the structural properties, open detector omega/2theta (002) X-ray diffraction (XRD) scans are performed. When TMIn is introduced as in Figure 16, the full-width-at-half-

maximum of the first and second order SL satellite peaks decrease significantly. All these results demonstrate that indium acts as a surfactant (indium incorporation is less than %2) and improves the overall SL quality using this technique.

3.4.3 Tunability of AlN and GaN Layers in the SL

Tunability of the well (GaN) and barrier (AlN) thickness are studied by growing AlN/GaN SL (as in Figure 18(a) inset) via varying the number of AlN pulses (steps (I) and steps (II)), GaN pulses (Steps (III) and (IV)) or the amount of GaN deposition time (for a single GaN pulse). XRD is used to characterize the SL. The angular separation between satellite peaks are used to calculate the SL period.[22] The average aluminum composition was calculated via $x_{Al} = \left(C_{AlGaN} - C_{GaN}^0\right)/\left(C_{AlN}^0 - C_{GaN}^0\right)$ where C_{GaN}^0 and C_{AlN}^0 are the free-standing lattice parameters of GaN and AlN, and C_{AlGaN} is the average lattice constant of the SL determined from X-ray analysis.[22]
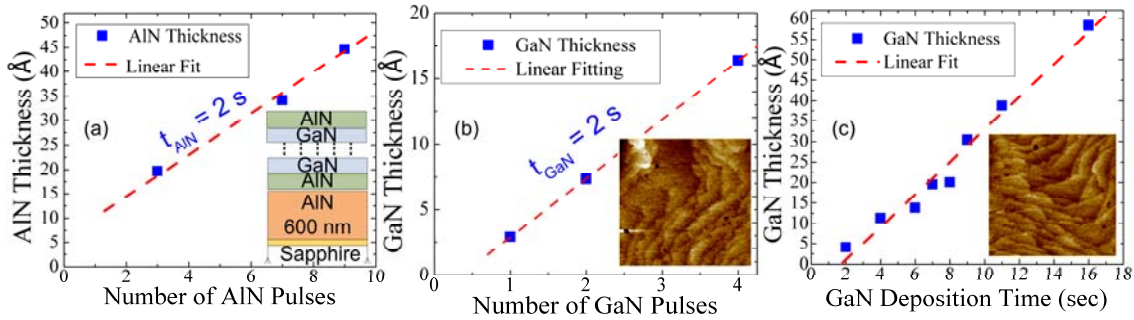

Figure 18: (a) AlN thickness versus number of AlN pulses for TMAl duration of 2 sec. Inset shows a cross-sectional diagram of a SL. (b) GaN thickness versus number of GaN pulses for TMGa duration of 2 sec. Inset shows the (1μm × 1μm) AFM SL surface without TMIn, (c) GaN thickness versus TMGa duration for a single GaN pulse. Inset shows the (1μm × 1μm) AFM SL surface with TMIn.

Fifty periods of various SL samples are grown, and layer thicknesses are deducted. The Figure 18(a) displays the AlN thickness dependency on number of AlN pulses. Similarly, GaN thickness dependency on GaN pulses and GaN deposition time are plotted in Figure 18(b) and (c), respectively. AlN (or GaN) thickness was found to be a linear function of AlN (or GaN) pulses. However, the linear fit to GaN thickness (Figure 18(b)(c)) intersect ordinate below abscissa which is attributed to the thinning of the GaN wells at high temperatures while AlN is being deposited.[18] Consequently, for the linear fit to AlN thickness (Figure 18(a)), the intersection with ordinate is above abscissa. However, a linear deposition growth rate with respect to AlN (or GaN) pulses and GaN deposition time is determined that makes this technique feasible for controllable AlN/GaN SL.

Realizing different ISB devices requires tunability of the individual well (GaN) layer for a constant barrier (AlN) thickness. Keeping the AlN barrier thickness at 3.1±0.2 nm, we have varied the GaN thickness as 0.8, 2.6 and 3.5±0.2 nm via changing the GaN deposition time

from 4, 9, and 11 seconds, respectively. XRD was employed to evaluate GaN and AlN thicknesses of the SLs. Fine satellite peaks were observed as shown in Figure 19 below.
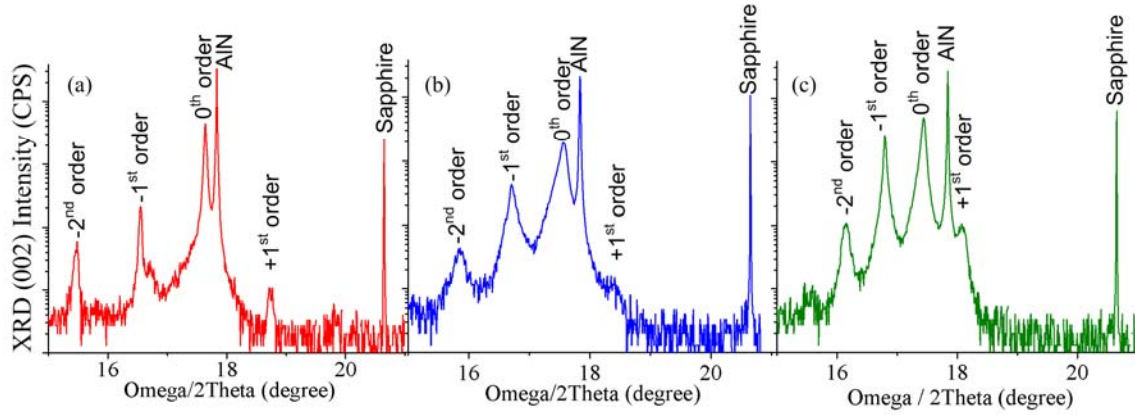
Figure 19: (002) Omega/2Theta XRD scans of (a) 50 periods of {0.8 nm GaN with 3.1 nm AlN} (b) 50 periods of {2.6 nm GaN with 3.1 nm AlN} (c) 50 periods of {3.5 nm GaN with 3.1 nm AlN}.

3.4.4 Effects of Doping on Optical and Structural Quality

Doping the well *n*-type is realized via the introduction of SiH_4 along with the metalorganic cation sources (Steps (I) and (III)). SLs with the same amount of dopants either in the barrier- or well- are grown and no significant structural differences were observed by XRD or AFM.
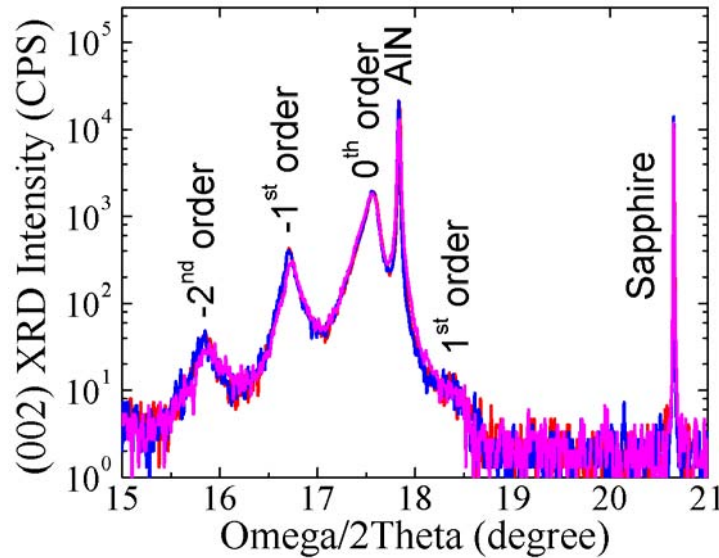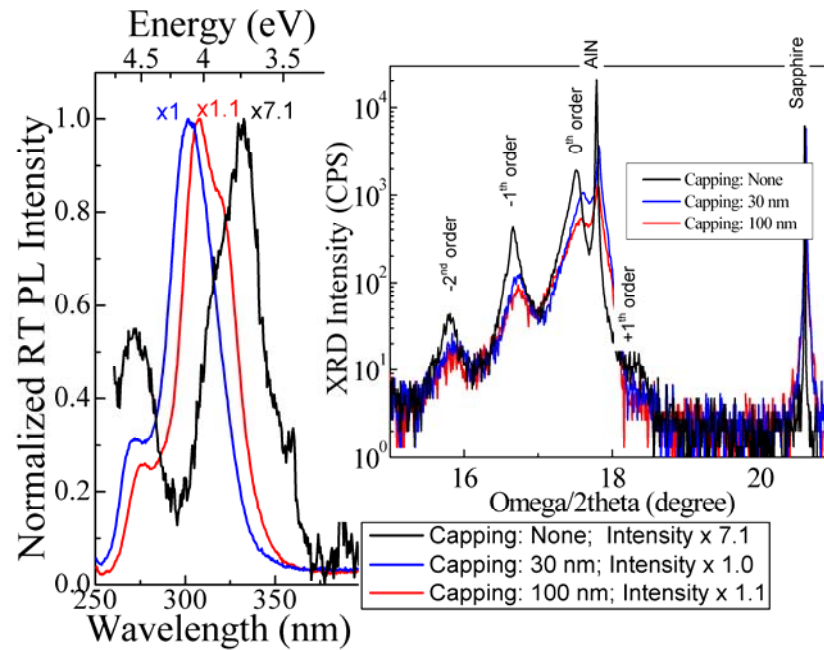

Figure 20 : (002) Omega/2Theta XRD of 50 period of {1.9 nm-thick GaN with 3.1-nm thick AlN} for different well n-doping levels.

In order to study the effect of doping on ISB absorption and assess the SL quality grown by our technique, we have grown 50 periods of {1.9 nm GaN with 3.1 nm AlN} SL on 600 nm AlN/c-sapphire with well doping levels of non-intentionally-doped $\sim 10^{16}$, slightly-doped 10^{17}, and highly doped 10^{19} cm^{-3}. Figure 20 above shows the (002) XRD Omega/2Theta scan for the SLs with different doping levels. No significant structural degradation with well-doping is observed.

### 3.4.5 Effects of Capping on the Optical and Structural Quality

The capping of the SL (50 periods of {1.8 nm-thick GaN / 3.1-nm thick AlN}) has been studied via photoluminescence (PL). Room temperature PL measurements are realized via frequency doubled Argon-Ion laser at 244 nm. Figure 21 shows the PL spectra of uncapped, 30, and 100 nm (AlN) capped SLs whereas inset shows the XRD (002) omega/2Theta scans. Uncapped SLs are crack-free whereas few edge cracks are observed for the 30 nm capping, and become more prominent for the 100 nm capping (not shown). Thus, the significant blue shift observed with increasing capping is attributed to partial strain relief via crack-formation. Consequently, XRD satellite peaks are better defined for (crack-free) uncapped sample with respect to (cracked) capped ones. With the crack-formation, no significant period change is observed, however, the 0th order peak of SL moved towards the AlN template peak – an indicator of strain relief occurring. The PL intensity increases for capped SLs, which we attribute to the partial doping effect via band-bending due to the AlN capping layer.[23]

Figure 21: Room temperature PL of 50 period {1.8 nm-thick GaN / 3.1 nm-thick AlN} SL with different AlN capping thicknesses (uncapped, 30, and 100 nm). Inset shows (002) omega/2theta XRD of the SL with the different capping thicknesses.

3.5. Effects of Growth Temperature and GaN Well Width on the Optical and Structural Quality

Room temperature photoluminescence (PL) measurements are realized via frequency doubled Argon-Ion laser at 244 nm. Figure 22 shows the room temperature PL intensity as a function of wavelength for 50 periods of {1.5-nm-thick GaN/3-nm-thick AlN} grown at three different T_S (900, 970, 1035ºC). A blueshift and an intensity decrease in PL with decreasing SL growth temperature are observed. Figure 22 inset displays the dependency of PL energy and intensity on GaN well width (for a constant 3.0-nm-thick AlN barrier). A decrease in PL energy and intensity is observed as well gets thicker. This behavior is characteristic of strained material. In a strained material, as the well thickness increases, the electron and hole wave functions are confined in the triangular part of the well due to the quantum-confined Stark effect. As a consequence, the overlap between the two wavefunctions decreases resulting in decreased recombination efficiency and thus PL intensity.
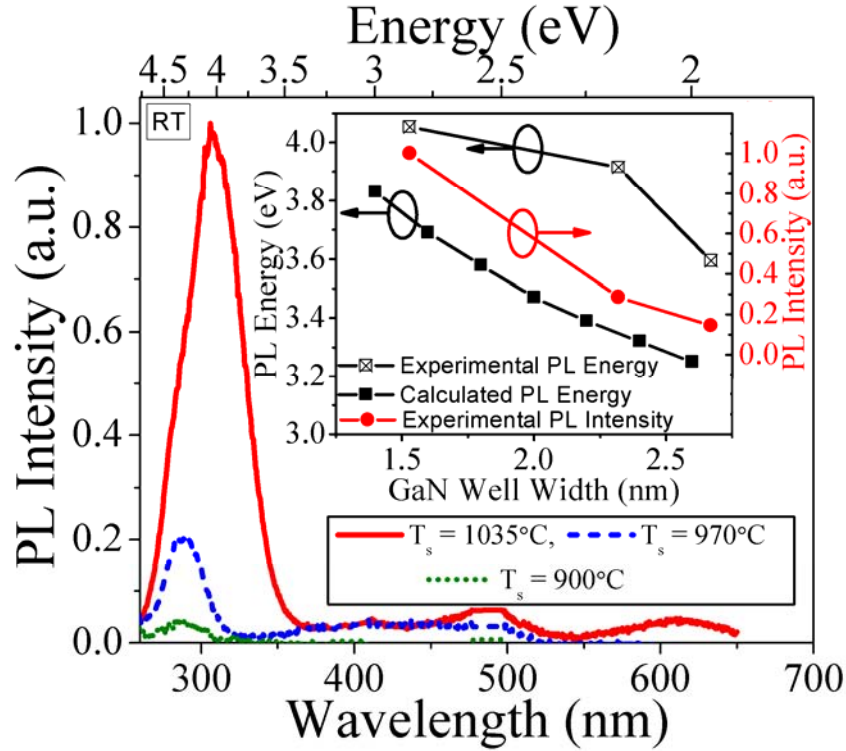
*Figure 22: Room temperature photoluminescence intensity as a function of wavelength for three different growth temperatures, 900, 970 and 1035•C for 50 periods of {1.5-nm-thick GaN/3-nm-thick AlN}. Wells are **n**-doped to 1×10^{18}cm^{-3}. Inset shows the experimental (and calculated) photoluminescence energy as a function of well width (for the same barrier thickness and growth temperature (T_S) of 1035•C).*

A theoretical model is developed to simulate inter- and intersub-band energy levels to compare with the experimental observations.[24] The model solves the Schrödinger equation taking into account the band non-parabolicity using the energy-dependent effective-mass approach in the highly strained band profile. Parameters used for the simulation are the

conduction and valence band offsets, the energy bandgap, and the strain. The strain is taken into account by applying an internal electric field to the wells and barriers. The superlattice is a periodic structure, thus the internal electric fields applied to the GaN wells and AlN barriers depends on the polarization discontinuity, and the well and barrier thicknesses.[25,26] Polarization constants for the binary well and barrier are taken from reference [27]. Figure 22 inset displays the experimental and theoretical PL energy as a function of the GaN well width. The interband simulations and PL experiments are in reasonably good agreement, however, a shift in energy between simulation and experiments is observed. This discrepancy of our experimental results with theory can be accounted for strain non-uniformities and interface quality. The simulation assumes a uniform strain across the structure whereas in reality, partial relaxations shall occur at the AlN-GaN interfaces leading to interfacial roughness. Another reason for interface degradation is GaN thinning, which will be addressed in the next sessions.
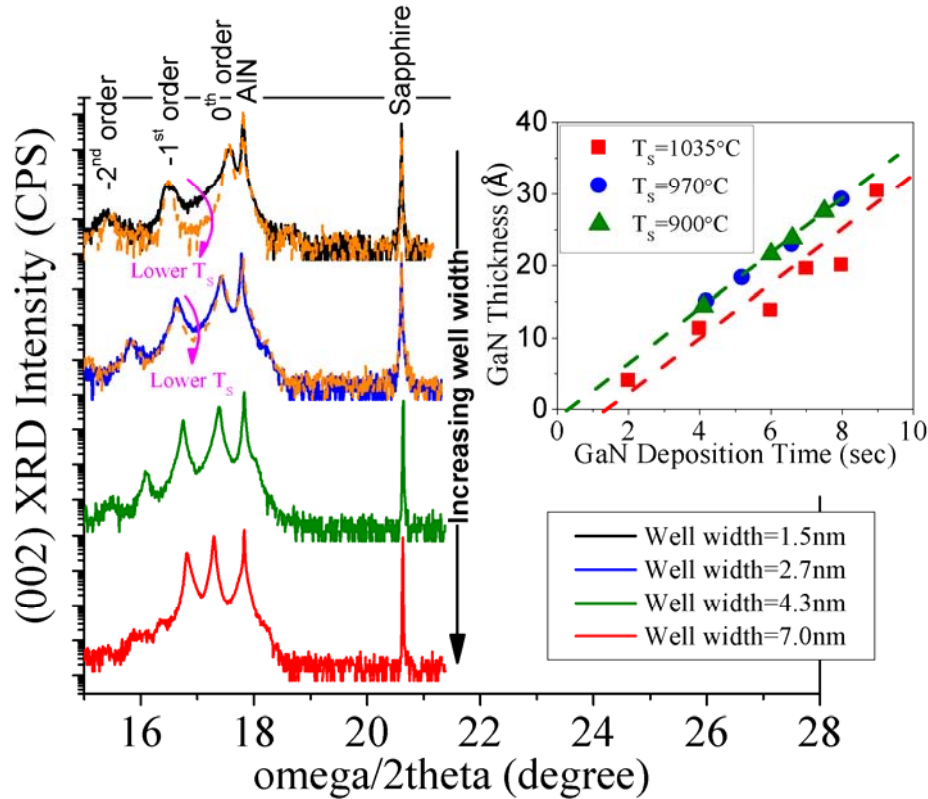
*Figure 23: (002) omega/2theta XRD of the SL with four well thicknesses (all **n-doped** of $1\times10^{18}cm^{-3}$) of 1.5, 2.7, 4.3 and 7.0 nm, employing 3-nm-thick barrier thickness. All SL are grown at growth temperature (T_S) of 1035°C (solid). The XRD of 1.5- and 2.7-nm-thick wells grown at 900°C are also shown (dashed). Inset shows the GaN thickness as a function GaN deposition time for three different growth temperatures, 900, 970 and 1035°C.*

X-ray diffraction studies were realized by high resolution Panalytical MPD-Pro system. Figure 23 shows the (002) omega/2theta XRD scans of the SLs with different well

thicknesses (1.5, 2.7, 4.3, and 7.0 nm) grown at 1035ºC (solid line). For the well thicknesses of 1.5 and 2.7 nm, XRD scans of SLs grown at 900ºC are also plotted. The satellite peaks are observed to be narrower for the SLs grown at lower T_S. Figure 23 inset displays the GaN thickness dependency on GaN deposition time. Fifty periods of various SL samples are grown, and layer thicknesses are deducted as follows: The angular separation between satellite peaks are used to calculate the SL period.[28] The average aluminum composition was calculated via $x_{Al} = \left(C_{AlGaN} - C_{GaN}^0\right)/\left(C_{AlN}^0 - C_{GaN}^0\right)$ where C_{GaN}^0 and C_{AlN}^0 are the free-standing lattice parameters of GaN and AlN, and C_{AlGaN} is the average lattice constant of the SL determined from X-ray analysis.[28]

The linear fit to GaN thickness (Figure 23 inset) at 1035ºC intersect ordinate below abscissa which is attributed to the thinning of the GaN wells at high temperatures while AlN deposition.[18] However, for SLs grown at 900 and 970ºC, linear fit to GaN thickness intersect ordinate almost at origin. These demonstrate that the interface quality is better for SLs grown at lower temperatures, mainly due to decrease in thinning of the GaN wells at lower temperatures.

3.6. Growth of AlGaN/GaN Superlattices

AlGaN/GaN SL are required to go further into the THz regime. Lower aluminum content of AlGaN should also enable lower strains, and higher quality. Figure 24 presents the complete tunability of AlGaN from pure AlN to GaN. Optical transmission and photoluminescence demonstrate the quality of the epilayer.
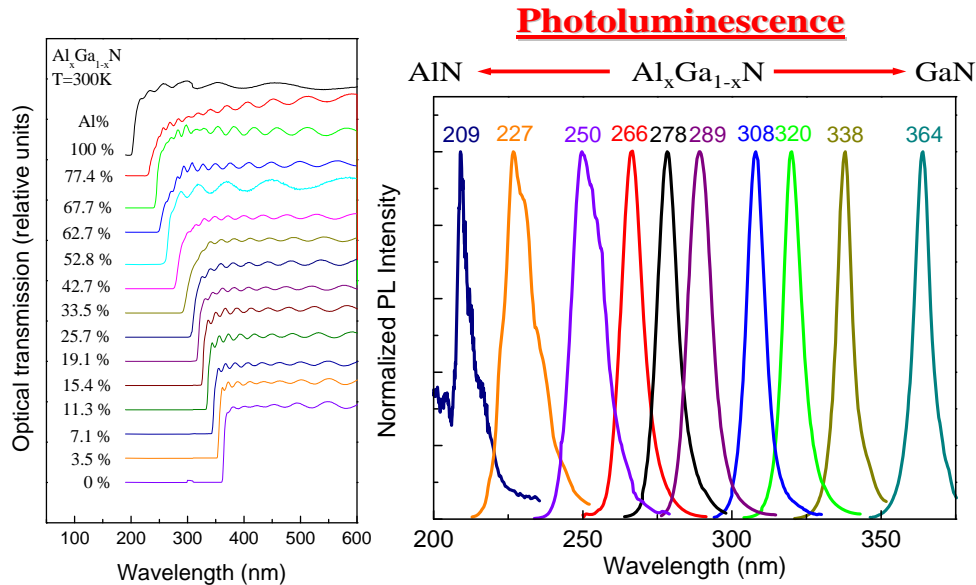
Figure 24: Left) UV Optical transmission of Al$_x$Ga$_{1-x}$N for different Al composition. Right) UV Photoluminescence of the samples. These figures demonstrates our complete tunability in the AlGaN range.

Figure 25 shows XRD and TEM of 13×{500Å $Al_{0.2}Ga_{0.8}N$ / 50Å GaN} on GaN/Sapphire. A high quality SL layer, many satellite peaks as well as sharp interfaces are observed.
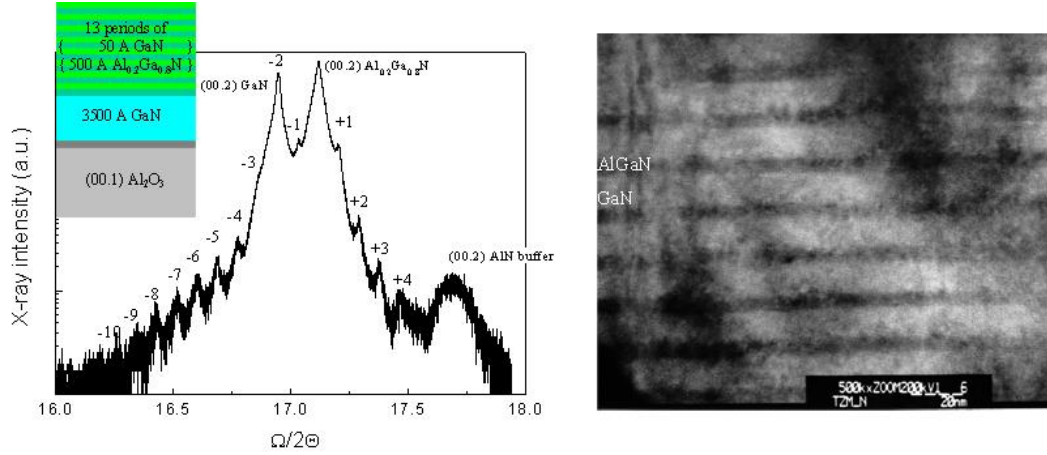
Figure 25: Left) XRD of 13×{500Å $Al_{0.2}Ga_{0.8}N$ / 50Å GaN} on GaN/Sapphire. Right) TEM of the SL sample. These figures demonstrate the high quality AlGaN/GaN SLs achieved.

In order to study the ISB transitions, several samples were grown with different well thicknesses (1.2 nm, 2.6 nm, 3.7 nm, and 5.1 nm) employing a constant barrier thickness of 2.9 nm. The active region consists of 50 periods of GaN wells with $Al_{0.2}Ga_{0.8}N$ barriers. All samples also have a 30 nm thick Al0.2Ga0.8N capping layer. The same structures were also grown with doped wells (Si: 1×1018 cm-3) to study the effects of doping.

In order to assess the structural properties of the superlattices, open detector omega/2theta (002) X-ray diffraction (XRD) scans are performed. Figure 26 represents the XRD plots for the four different well thicknesses. In Figure 26, the narrowest peak located at 20.7° corresponds to sapphire substrate, the peak at 18.2° corresponds to AlN, and the 0th order and 1st order superlattice peaks are also present. The average aluminum composition was calculated from the angular difference between the AlN peak and the 0th order of the superlattice. [29] Once the average aluminum content was determined, we extracted the period of the superlattice from the spacing of satellite peaks.[30] The inset of Figure 27 shows the calculated superlattice period as a function GaN growth time. By varying the GaN growth time (and keeping the AlGaN barrier thickness constant), a linear change in the GaN well width is observed, from the slope of which a GaN growth rate of 0.64 Å/s is extracted. The y-intercept then corresponds to the barrier thickness (which was held constant), evaluated to be 2.9 nm. By using this fixed barrier thickness together with the superlattice period and average composition, we are able to confirm the aluminum composition in the $Al_{0.20}Ga_{0.80}N$ barriers.
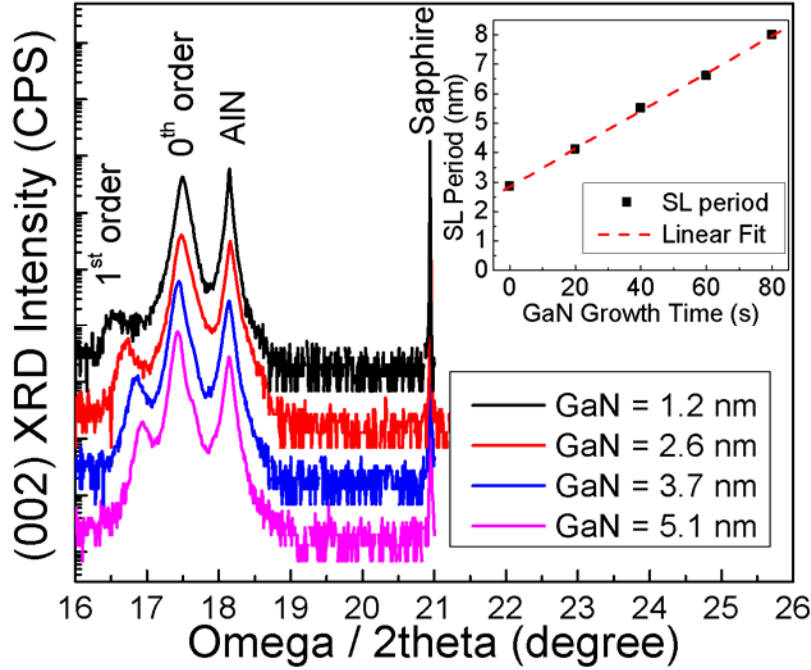
Figure 26: Omega/2theta (002) X-Ray diffraction (XRD) of superlattices with four different well thicknesses: from top to bottom these are 1.2 nm, 2.6 nm, 3.7 nm and 5.1 nm GaN. Wells are Si doped to 1×10^{18} cm^{-3}. The barriers for all samples are 2.9 nm-thick $Al_{0.2}Ga_{0.8}N$. Inset: superlattice period (from XRD analysis) as a function of well growth time is used to extract the GaN growth rate and determine the well thicknesses.

Photoluminescence (PL) measurements were performed at room temperature using a frequency-doubled argon-ion laser emitting at 244 nm for excitation. The peak PL energy corresponds to the fundamental interband transition in the multi-quantum-well structure. Figure 28 plots the PL intensity as a function of energy for 1.2 nm, 2.6 nm, 3.7 nm, and 5.1 nm GaN well thicknesses (wells are Si doped 1×1018cm-3) and 2.9 nm Al0.2Ga0.8N barrier (barriers are undoped). As expected, a redshift of PL emission is observed as the well thickness increases and the confined electron and hole states move towards the bottom of the wells. As the well width increases, the PL shifts until the sample with 5.1 nm thick well, it exhibits peak PL emission at 3.33 eV. Generally the bulk bandgap energy of GaN is taken to be 3.44 eV.[1] In the case of these $Al_{0.2}Ga_{0.8}N$/GaN superlattices, the peak PL emission energy is below the bandgap energy due to the strain in the material. In addition, the intensity of the PL emission decreases significantly with increasing well width; this behavior is also characteristic of strained material. In a strained material, as the well thickness increases, the electron and hole wave functions are confined in the triangular part of the well due to the quantum confined Stark effect. As a consequence, the overlap between the two wave functions decreases resulting in decreased recombination efficiency and thus PL intensity. A Gaussian fit was performed on the PL emission peaks revealing a full width at half maximum (FWHM) for the 1.2 nm, 2.6 nm, 3.7 nm, and 5.1 nm GaN well thicknesses of 111.5 meV, 102.5 meV, 127.5 meV, and 172.5 meV, respectively. The FWHM tends to increase with

31

well-width except for a minor inconsistency for the first two FWHM values, likely due to inhomogeneous broadening from such thin well widths. These FWHM values are sufficiently narrow so as to imply good quality of the superlattice material grown. The quality of the sample is also highlighted by the absence of any yellow peak in the PL emission, generally attributed to nitrogen vacancies or impurities.
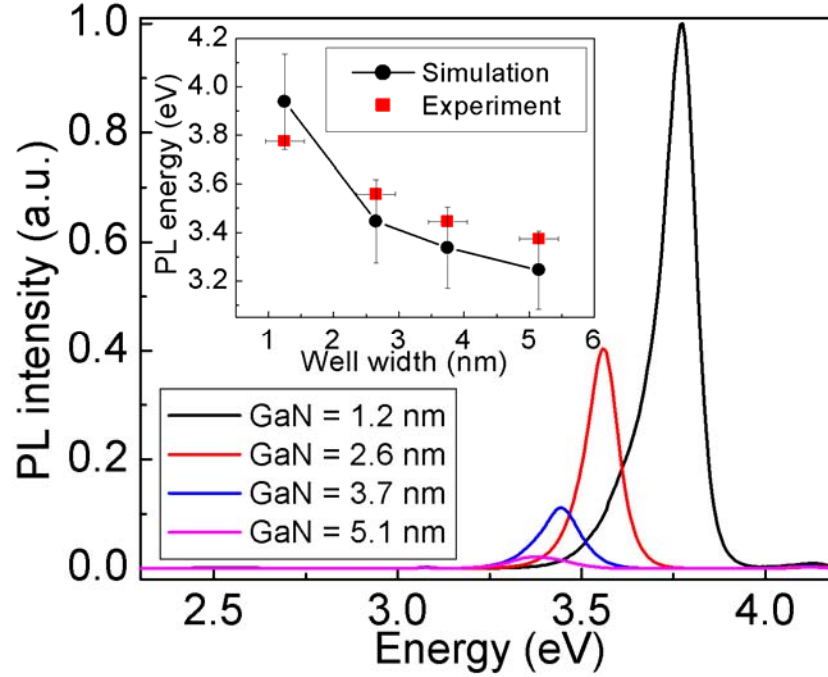
Figure 27: Photoluminescence (PL) intensity as a function of energy for four different GaN well thicknesses: 1.2 nm, 2.6 nm, 3.7 nm, and 5.1 nm – all with a constant 2.9 nm Al$_{0.2}$Ga$_{0.8}$N barrier thickness. Superlattice consists of 50 periods where each well is Si doped to 1×10^{18} cm^{-3}. Inset: Comparison theory/experiment photoluminescence energy as a function of well width.

In order to interpret the PL results, we performed simulations of the electron and hole confinement in the conduction and valence bands. We solved the Schrödinger equation taking into account the band non-parabolicity using the energy-dependent effective-mass approach in the highly strained band profile. Parameters used for the simulation are the conduction and valence band offsets, the energy bandgap, and the strain. The strain is taken into account by applying an internal electric field to the wells and barriers. A rough estimation of the strain is achieved via linear interpolation of the constants used for binary/binary SLs. The superlattice is a periodic structure, thus the internal electric fields applied to the GaN wells and Al$_{0.2}$Ga$_{0.8}$N barriers depends on the polarization discontinuity, and the well and barrier thicknesses. Polarization constants for the binary well and for the ternary barrier are taken from reference [27]. The inset of Figure 27 displays the experimental and theoretical PL energy as a function of the GaN well width. The interband simulations and PL experiments are in reasonably good agreement, however, a shift in wavelength between simulation and

experiments is observed. This slight discrepancy of our experimental results with theory and with experimental results reported in reference [31] can be accounted for by uncertainties in the layer thicknesses (error bars one monolayer (ML)) and strain in the AlGaN/GaN structure (error 5%). Indeed, the simulation assumes the structure is fully strained with respect to the barrier material ($Al_{0.2}Ga_{0.8}N$) whereas in the real structure there may partial relaxation occurring at the $Al_{0.2}Ga_{0.8}N$ on GaN interfaces, interfacial roughness, or incomplete relaxation at the AlGaN/AlN template interface. Further investigations, like XRD reciprocal space mapping may be able to provide a better estimate of the true strain.

We also performed the same PL experiments for the undoped samples. These samples have the same superlattice structure as the doped samples, however there is a slight redshift in PL emission with respect to the doped samples. This shift to lower energy for the undoped samples can be attributed to the partial carrier screening of the internal electric field.

3.7. Intersubband Absorption and Discussion

Samples were prepared for ISB absorption measurements by dicing to allow transverse optical access to the layers. Broad-band light from a blackbody source, either p- or s-polarized, was incident perpendicular to one side facet of the samples, traveled along the SL region and went out from the other facet. The infrared transmission was measured at room temperature using a Fourier transform infrared spectrometer (FTIR). The difference between the absorption of p- and s-polarized light was used to identify the ISB absorption.

### 3.7.1 Effect of capping thickness and doping on ISB absorption

Figure 28 displays the transmission of the p-polarized light for uncapped, 30, and 100 nm capped SLs, as well as undoped, well-doped, or barrier-doped samples. For uncapped samples, a weak absorption is observed. With 30 nm capping, the absorption is significantly increased. This is attributed to the unintentional doping generated by band bending with AlN capping,[23] and supports the increase in PL intensity observed. With thicker capping (100 nm), the absorption increased further. However, the strain relaxation via cracking is believed to lower the ISB transition energy causing a red-shift (Figure 28). Irrespective of *n*-doping in barrier or well, ISB transition energy increased (blueshifted) with the addition of doping, due to many-body effects.[23] In conclusion, ISB absorption as low as 1.53 µm - the lowest wavelength reported by MOCVD - is realized and this technique is shown to be appropriate for near-infrared intersubband absorption.
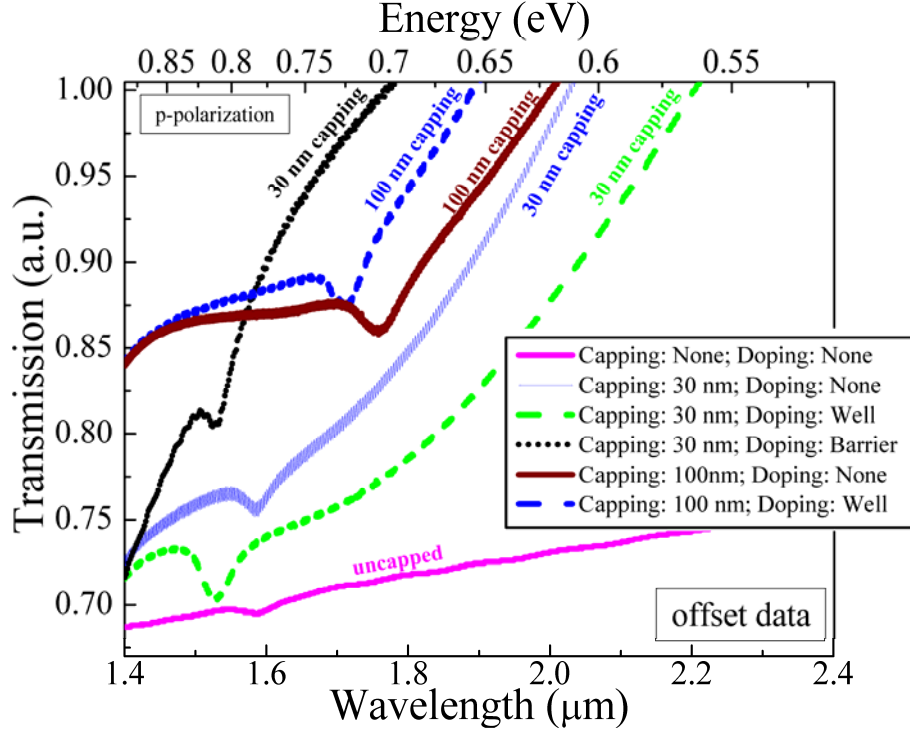
Figure 28: Relative (p-polarization) transmission of undoped, well- or barrier-doped, and uncapped, 30 or 100 nm capped 50 period {1.8 nm-thick GaN / 3.1-nm thick AlN} SL.

3.7.2 Effect of Growth Temperature on ISB absorption

Samples were prepared for ISB absorption measurements by dicing to allow transverse optical access to the layers. P- or s- polarized white light was incident perpendicular to one side facet of the samples, traveled along the SL region and went out from the other facet. The infrared transmission was measured at room temperature using a Fourier transform infrared spectrometer. The difference between the absorption of p- and s-polarized light was used to identify ISB absorption. Figure 29 displays the (p-polarized) transmission of the SLs with well widths of 1.5, 2.2 and 2.7 nm (with AlN barrier width of 3.0 nm). Figure 29 shows that lower T_S results in a higher ISB absorption energy, and a narrower absorption feature. Figure 29 inset shows the effect of T_S and well width on ISB energy. Wider wells and higher T_S lead to lower intersubband energies. Wider wells decrease the separation between first and second electronic state leading to lower ISB energy.
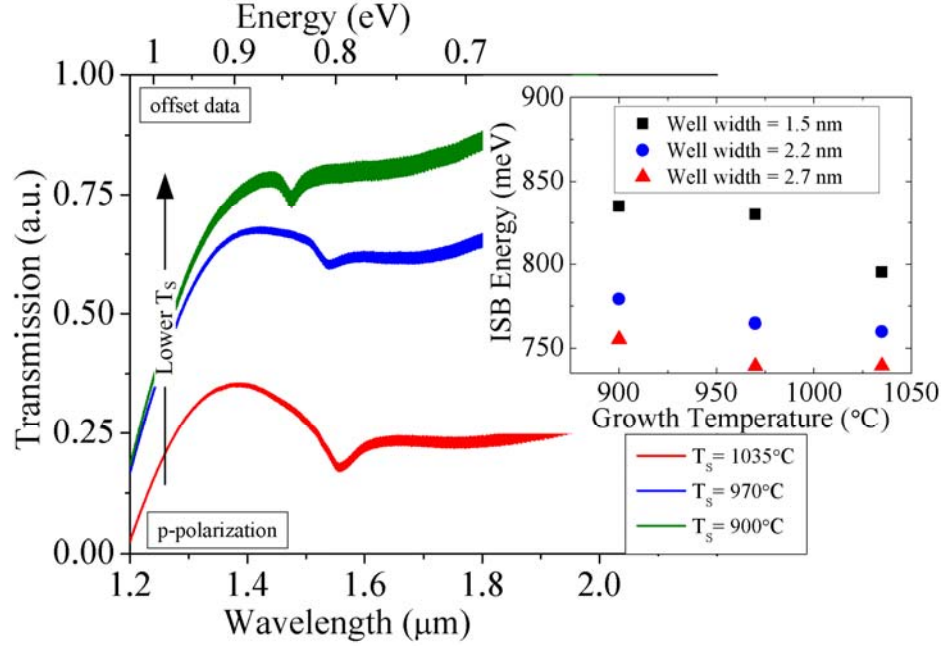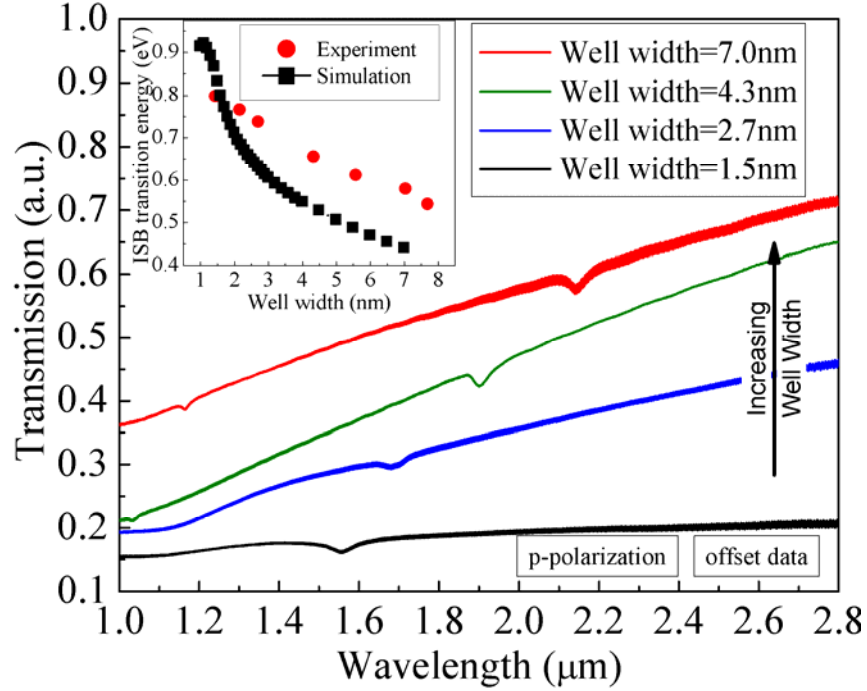
Figure 29: Transmission as a function of wavelength for three different growth temperatures, 900, 970 and 1035°C for 50 periods of {1.5-nm-thick GaN/3.0-nm-thick AlN}. Wells are doped to 1×1018cm-3. Inset shows intersubband transition energy as a function of growth temperature for well thicknesses of 1.5, 2.2, and 2.7 nm.

3.7.3 Effect of Well Width on ISB absorption

Figure 30 displays the (p-polarized) transmission of the SLs with well widths of 1.5, 2.7, 4.3, and 7.0 nm. The absorption feature (attributed to transition from first to second electronic state) redshifts with increasing well width. This is related to electron states getting closer to the each other as the well gets thicker. For wells of 4.3 and 7.0 nm, another absorption feature with higher energy is observed. This is attributed to the transition from the first to the third electronic state. With the varying well width, intersubband absorption is tuned from 1.5 to 2.2 µm.

The ISB absorption wavelength as a function of well width was simulated; a comparison with the experimental data is shown in Figure 30 inset. The simulation data is in a good harmony with the experimental one for thinner wells, however, as the well width increases, simulated and experimentally-measured ISB energies begin to differ. This could be attributed to degradation in SL quality for thickest wells. When XRD scans of SLs with 1.5- through 7.0-nm-thick wells are compared (in Fig. 3), it is noticed that satellite peaks get narrower from 1.5- through 4.3-nm-thick ones, but degrades for 7.0-nm-thick one. This is related to growing GaN thicker than critical thickness in AlN/GaN SL. The discrepancy of our experimental data with the simulation one can be accounted for strain non-uniformities in and interface quality of the SL.

Figure 30: Transmission as a function of wavelength for four well thicknesses of 1.5, 2.7, 4.3 and 7 nm. For all cases, AlN barrier thickness and growth temperature is 3.0 nm and 1035ºC, respectively. Inset shows theoretically-calculated and experimentally-observed ISB absorption energies as a function of well width (for the transition from the first state to the second state where other transitions are possible).

The effect of n-type doping on SLs and its dependence on T_S is investigated via growing doped and undoped SLs. No significant structural differences are observed by XRD or atomic force microscopy for AlGaN/GaN SL samples (not shown), similar to our previous work.[1, 2]

In summary, AlN/GaN SLs grown at lower T_S are shown to have less thinning of the GaN well and to possess narrower XRD satellite peaks. Higher T_S and wider wells decrease PL energy and the ISB absorption energy of AlN/GaN SLs. Well width and the growth temperature are shown to be key parameters for AlN/GaN SLs absorbing in near-infrared. Theoretical modelling and simulations are realized to validate experimental observations.

3.7.4 Intersubband Absorption in GaN/AlGaN SLs up-to 5.3 µm

Intersubband absorption measurements were realized using a Bruker IFS 66V vacuum Fourier Transform Infrared spectrometer, with an internal blackbody source, and a cryogenic mercury-cadmium-telluride detector. Samples were cut into 4 mm long bars and 45° angle facets were polished on both sides in order to form a multipass waveguide. A wire-grid polarizer was inserted into the beam-path just before the sample to select either p- or s-polarization for the incident light. Figure 31(a) presents both p-polarization (solid line) and s-polarization (dashed line) raw transmission data for the sample with doped 2.6 nm wells and 2.9 nm barriers. For both polarizations, we observe 100% absorption above $\lambda = 6.1$ µm – this

is attributed to absorption in the sapphire substrate. This absorption represents a significant limiting factor in the development of longer wavelength devices. An absorption edge is also observed in the *p*-polarization at a wavelength of 4.5 µm whereas no corresponding absorption is observed for *s*-polarization verifying this feature as ISB absorption. For the well width of 1.2 nm, no ISB absorption feature is observed; this agrees with theory as only one bound state is present in this well, and thus no ISB absorption should occur. For the remaining three well widths, the negative logarithm of the ratio of the two spectra (*p*-polarization and *s*-polarization) normalized by the open beam are plotted in Figure 31(b), this corresponds to the ISB absorbance. The ISB absorbance peaks at 4.5 µm, 4.9 µm, and 5.3 µm for the 2.6 nm, 3.7 nm, and 5.1 nm well widths, respectively. The increasing well width redshifts the ISB absorption peak as the two first confined states of the well become closer in energy. For the 2.6 nm thick well we observe a broader absorption peak compared to the two wider wells (3.7 and 5.1 nm). For the 2.6 nm well width, some oscillations appear around 6 µm in the absorbance, these are attributed to the normalization with s-polarized spectra close to the sapphire cut-off. For each of the two wider wells we observe one prominent absorption feature that can be fitted with Lorentzian functions (dashed lines), characteristic of ISB transitions. Lorentzian functions do not perfectly fit the experimental curves around 6 µm due to the normalization. Furthermore, the decrease of ISB absorption intensity as the well width increases is explained by the decrease of quantum confinement for the second subband compared to the fundamental state reducing the optical dipole matrix element.
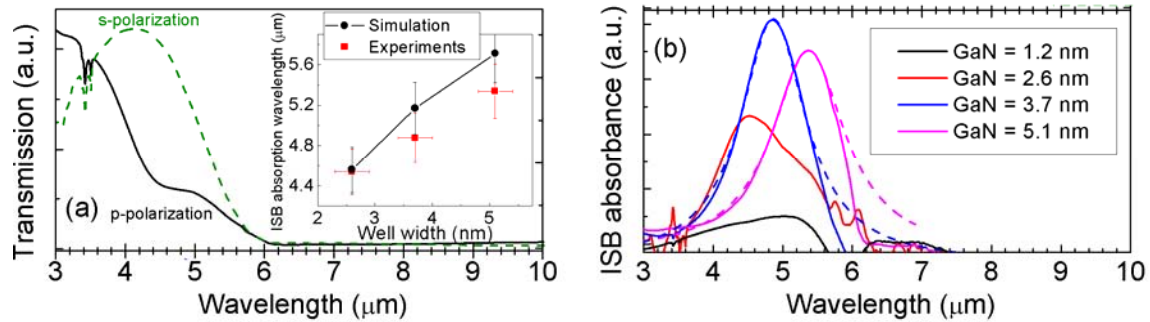
Figure 31: (a) Solid line is the* p*-polarization transmission for 2.6 nm well width and 2.9 nm barrier with, wells are Si doped to 1×10^{18} cm^{-3}, the dashed line corresponds to* s*-polarization transmission for the same sample. Inset: ISB absorption wavelength as a function of well width – experimental results (squares) and simulation (circles) for a fully strained structure. (b) From left to right, ISB absorbance for 2.6 nm (red), 3.7 nm (blue), and 5.1 nm (magenta) well widths. Lorentzian fits are shown (dashed lines) for the 3.7 and 5.1 nm well widths.

The ISB absorption wavelength as a function of well width was simulated; a comparison with the experimental data is shown in the inset of Figure 31(a). A very good fit is obtained for the thinnest well (2.6 nm), but the discrepancy increases as the well width increases. It may be explained by the variation behavior of the background and then, the normalization (error 5%). Plus, this discrepancy is attributed to uncertainties in internal electric field and conduction band offset as the two subbands are located in the triangular part

of the well for thicker wells (error 5%). Further studies of these two parameters are required to minimize this discrepancy.

In summary, AlGaN/GaN SLs absorbing from 4.5 to 5.3 µm were also grown, processed, and characterized. Effects of growth temperature, well width, doping, and capping were studied. RTD and QWIP designs based on AlN/GaN and AlGaN/GaN were developed, tested, and are still being pursued. Optical and electrical pumping designs were developed from mid-infared to THz range. 5.3 µm is the longest III-Nitride based intersubband absorption wavelength either by MBE or MOCVD. Longer wavelengths are not possible without using alternative substrates due to the absorption cutoff at 6 µm of the sapphire substrate.

3.7.5 Multi-pass Geometry

Another setup is multi-pass structure that uses 45 degrees multipass waveguide (Figure 28), and has been studied in order to achieve higher absorption. Samples were polished in a holder using grinding, lapping and polishing disk with diamond suspension from 45 µm to 1 µm. Light is sent through one edge and reflects multiple time inside after which it is ejected form the other polished facet. The measurements setup is still being improved to reproduce results with polished samples. Polishing has been carefully achieved as light diffusion may be one of the reasons for the initial difficulties realizing absorption using the multi-pass geometry. With processing optimization, smooth surface has been realized as can be seen in Figure 33.
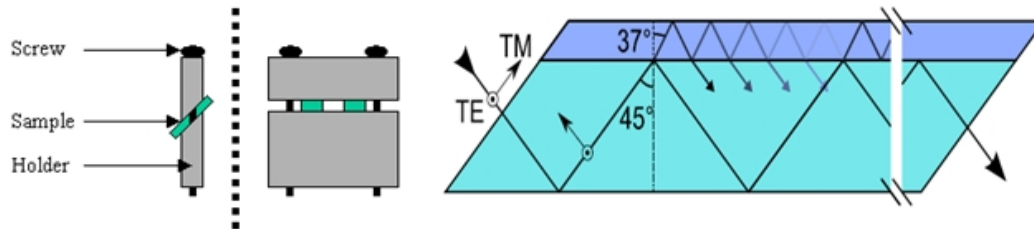
Figure 32: 45 Degrees multi-pass waveguide
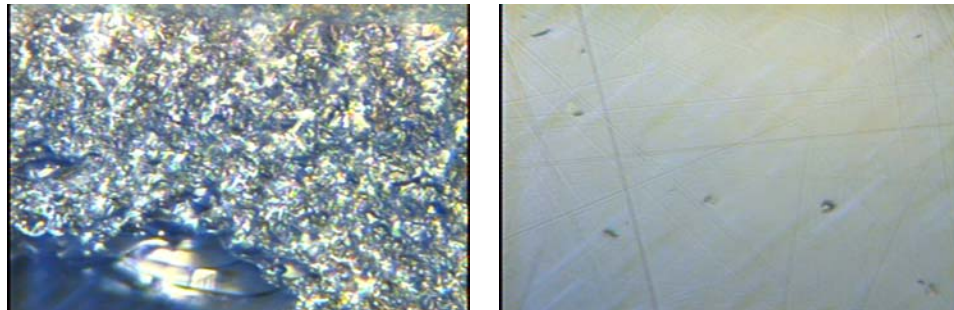
Figure 33: Sample edge before and after polishing (optical micrograph).

3.8. Conclusion

In summary, a pulsed MOCVD deposition technique for high optical and structural quality AlN/GaN SL is introduced. Indium is shown to improve the surface and structural quality. Tunability of AlN and GaN thicknesses is demonstrated. Intersubband absorption at 1.53 µm is achieved at room temperature, via MOCVD grown material. Lower (red-shift) and higher ISB transition energy (blue-shift) is observed in strain-relaxed and well- or barrier-doped SLs, respectively. AlN/GaN SLs grown at lower T_S are shown to have less thinning of the GaN well and to possess narrower XRD satellite peaks. Higher T_S and wider wells decrease PL energy and the ISB absorption energy of AlN/GaN SLs. Well width and the growth temperature are shown to be key parameters for AlN/GaN SLs absorbing in near-infrared. Theoretical modelling and simulations are realized to validate experimental observations.

We have studied $Al_{0.2}Ga_{0.8}N$/GaN superlattices grown by MOCVD with various well thicknesses via XRD, PL, and polarization dependant ISB absorption measurements. A theoretical model was developed taking into account strain in binary/ternary superlattices to correlate with both experimental interband emission and ISB absorption results. Ultimately we demonstrate tunability of ISB absorption from 4.5 to 5.3 µm in a $GaN/Al_{0.2}Ga_{0.8}N$ superlattice. ISB absorption was demonstrated in the wavelength range of 1.53 µm to 5.3µm. These demonstrations are important steps towards employing GaN/AlGaN SLs in longer wavelength ISB devices.

4. Conclusion and Future Work

4.1. Conclusion

We presented in the status of the simulation and design portion of the work and laid out a road map for continued development. We will work on ISB emission experiments by optical pumping in GaN/AlGaN material. This experiment/simulation part needs to be carried out closely with the material counterpart in order to provide close feedback between the two components. In each part of the report, we presented the importance of the experimental results.

The physics of a quantum cascade laser needs to be well understood as a whole to realize such a device. The three parts, injection, emission and extraction are currently being studied. The injection is via design and experiments of resonant tunneling. The emission is by both absorption theory and design and for the moment emission by different designs by optical pumping. The extraction is also already studied by developing optical pumping designs to bring the carriers out of the lower subband. The increase of the wavelength is in the same time carried out with different design in absorption and optical pumping.

From the standpoint of growth, a novel pulsing technique has been developed to realize high-quality superlattices by MOCVD that successfully demonstrated intersubband absorption at 1.53 µm. This is world's lowest wavelength ISB transition ever achieved by MOCVD. We

have This has proved MOCVD as a reliable deposition technique for Nitride ISB devices. Doping is shown to blueshift the ISBTs. Besides, strain-relief via crack-formation is observed to red-shift the ISBTs. The correlation between material growth & characterization and theoretical predictions are studied. In summary, high quality GaN/AlN SLs are realized demonstrating the strong capabilities of MOCVD as a promising deposition technique for THz. We have studied $Al_{0.2}Ga_{0.8}N$/GaN superlattices grown by MOCVD with various well thicknesses via XRD, PL, and polarization dependant ISB absorption measurements. A theoretical model was developed taking into account strain in binary/ternary superlattices to correlate with both experimental interband emission and ISB absorption results. Ultimately we demonstrate tunability of ISB absorption from 4.5 to 5.3 µm in a GaN/$Al_{0.2}Ga_{0.8}N$ superlattice. This demonstration is an important step towards employing GaN/AlGaN SLs in longer wavelength ISB devices.

4.2. Future Work

AlGaN layers specifically designed for longer wavelengths will be realized and integrated into AlGaN/GaN SLs. Growth on both polar and non-polar free-standing GaN substrates will be realized. Resonant tunneling diode based on AlGaN/GaN structure will be achieved as well. Good quality interfaces should be slightly easier to realize since the lattice mismatch is reduced. Processing including photolithography, etching and metal deposition will also be optimized for THz lasers. A contact study will be realized in order to reach a low specific contact resistance ($\rho < 10^{-5}$ $\Omega.cm^2$). Metals, metals thicknesses and annealing temperature will be optimized using Transmission Line Measurements (TLM). Ti/Al/Ni/Au are the most promising contact but Ti/Au and Ti/Al/Au/Ti/Au will be studied as well.[20]

We will investigate free-standing polar and non-polar substrates for defect reduction. AlGaN/GaN interfaces will be improved by defect reduction and growth optimization. We will demonstrate resonant tunneling in an AlGaN/GaN structure grown by MOCVD. After that, absorption in the THz regime in AlGaN/GaN structures will be realized. Infrared and THz emission by optical pumping in AlGaN/GaN multi-quantum-well structures will be investigated. Growth on polar and non-polar GaN substrates will be realized for higher quality AlGaN/GaN SLs and to facilitate THz laser processing. We will develop THz laser processing including wafer bonding, substrate removal, and metal waveguide. We will conclude with the demonstration of electroluminescence from AlGaN/GaN laser structures.

Meanwhile, theoretical approach of more complex devices such as detector and later quantum cascade laser will be realized. We likely will develop a design based on a depopulation by LO phonon. Theoretical comparison between devices grown on polar substrate and devices grown on non-polar substrate will be done. This will require a more powerful solver taking into account Poisson field and many-body effects such as depolarization excitonic shift.

5. References

[1] C. Bayram, N. Péré-Laperne, and M. Razeghi, *Appl. Phys. Lett.* (under review).

[2] C. Bayram, B. Fain, N. Péré-Laperne, R. McClintock, and M. Razeghi, *Proc. SPIE* **7222**, 722212 (2009).

[3] C. Bayram, N. Péré-laperne, R. McClintock, B. Fain, and M. Razeghi, *Appl. Phys. Lett.* **94**, 121902 (2009).

[4] N. Péré-Laperne, C. Bayram, L. Nguyen-Thê, R. McClintock, and M. Razeghi, *Appl. Phys. Lett.* **95**, 131109 (2009).

[5] Norio Iizuka, Kei Kaneko, Nobuo Suzuki, Takashi Asano, Susumu Noda and Osamu Wada *Appl. Phys. Lett.* 77, 648 (2000)

[6] D. Hofstetter, L. Diehl, J. Faist, W. J. Schaff, J. Hwang, L. F. Eastman, and C. Zellweger *Appl. Phys. Lett.* 80, 2991 (2002)

[7] P.K. Kandaswamy, F. Guillot, E. Bellet-Amalric, E. Monroy, L. Nevou, M. Tchernycheva, A. Michon, F.H. Julien, E. Baumann, F.R. Giorgetta, D. Hofstetter, T. Remmele, M. Albrecht, S. Birner, and Le Si Dang, *J.Appl. Phys.* **104**, 093501 (2008).

[8] H. M. Ng *Appl. Phys. Lett.* 80, 4369 (2002)

[9] C. Gmachl and H. M. Ng, *Elect. Lett.* **39**, 567 (2003)

[10] L. Nevou, M. Tchernycheva, F. H. Julien, F. Guillot and E. Monroy *Appl. Phys. Lett.* 90, 121106 (2007).

[11] R. Ferreira and G. Bastard, *Phys Rev B* **40**, 1074 (1989)

[12] A. Kikuchi, R. Bannai, K. Kishino, C.-M. Lee and J.-I. Chyi, *Appl. Phys. Lett.* 81, 1729 (2002)

[13] C. Bayram, J. L. Pau, R. McClintock, and M. Razeghi, *J. Appl. Phys.* **104**, 083512 (2008).

[14] A.D. Bykhovski, B. L. Gelmont, and M.S. Shur, *J. Appl. Phys.* **81**, 6332 (1997).

[15] N. Suzuki, N. Iizuka, and K. Kaneko, *Jpn. J. Appl. Phys.* **42,** 132 (2002).

[16] C. Adelmann, E. Sarigiannidou, D. Jalabert, Y. Hori, J. –L. Rouviere, B. Daudin, S. Fanget, C. Bru-Chevallier, T. Shibata, and M. Tanaka, *Appl. Phys. Lett.* **82**, 4154 (2003).

[17] P. Boguslawski, K. Rapcewicz, and J.J. Bernholc, *Phys. Rev. B* **61** 10820 (2000).

[18] N. Gogneau, D. Jalabert, E. Monroy, E. Sarigiannidou, J.L. Rouviere, T. Shibata, M. Tanaka, J.M. Gerard, and B. Daudin, *J. Appl. Phys.* **96**, 1104 (2004).

[19] S. Nicolay, E. Feltin, J. –F. Carlin, N. Grandjean, L. Nevou, F.H. Julien, M. Schmidbauer, T. Remmele, and M. Albrecht, *Appl. Phys. Lett.* **91**, 061927 (2007).

[20] C. H. Chen, H. Liu, D. Steigerwald, W. Imler, C.P. Kuo, and M.G. Craford, *J. of Electron. Mater.* **25**, 1004 (1996).

[21] H.J. Kim, S. Choi, D. Yoo, J. –H. Ryou, R.S. Dupuis, R.F. Dalmau, P. Lu, and Z. Sitar, *Appl. Phys. Lett.* **93**, 022103 (2008).

[22] S. Zhou, M.F. Wu, S.D. Yao, B.S. Zhang, and H. Yang, *Superlattices and Microstructures* **40**, 137 (2006).

[23] P.K. Kandaswamy, F. Guillot, E. Bellet-Amalric, E. Monroy, L. Nevou, M. Tchernycheva, A. Michon, F.H. Julien, E. Baumann, F.R. Giorgetta, D. Hofstetter, T. Remmele, M. Albrecht, S. Birner, and Le Si Dang, *J.Appl. Phys.* **104**, 093501 (2008).

[24] N. Péré-laperne, C. Bayram, L. Nguyen-Thê, R. McClintock, and M. Razeghi (submitted).

[25] D. Vanderbilt and R. D. King-Smith, *Phys. Rev. B* **48**, 4442 (1993).

[26] M. Leroux, N. Grandjean, J. Massies, B. Gil, P. Lefebvre, and P. Bigenwald, *Phys. Rev. B* **60**, 1496 (1999).

[27] I. Vurgaftman, and J.R. Meyer, *J. Appl. Phys.* **89**, 5815 (2001).

[28] S. Zhou, M.F. Wu, S.D. Yao, B.S. Zhang, and H. Yang, *Superlattices and Microstructures* **40**, 137 (2006).

[29] S. Zhou, M.F. Wu, S.D. Yao, B.S. Zhang, and H. Yang, *Superlattices and Microstructures* **40**, 137 (2006).

[30] M. A. Moram and M. E. Vickers, *Rep. Prog. Phys.* **72,** 036502 (2009).

[31] N. Grandjean, J. Massies, and M. Leroux. *Appl. Phys. Lett.* **74**, 2361 (1999).